Angewandte Chemie
Eine Zeitschrift der Gesellschaft Deutscher Chemiker

Supporting Information

Enantiomeric Discrimination by Surface-Enhanced Raman Scattering–Chiral Anisotropy of Chiral Nanostructured Gold Films

Zexi Liu[+], Jing Ai[+], Prashant Kumar[+], Enming You[+], Xiong Zhou[+], Xi Liu[+], Zhongqun Tian, Petr Bouř, Yingying Duan, Lu Han,* Nicholas A. Kotov,* Songyuan Ding,* and Shunai Che**

ange_202006486_sm_miscellaneous_information.pdf

Supporting Information
Experimental Section

Preparation of CNAF

In a typical synthesis of R-CNAF, the lithographically ablated silicon wafer (1cm×4 cm) with cylinder holes (diameters of 1 mm and depth of 1 mm) was firstly activated with H_2SO_4/H_2O_2 mixed solution for 2 hours and then immersed in 50 mM APTES solution for 2 hours to modify amino groups on the surface. Then, 3.45 mM S-NAC, 5.52 mM 4-MBA and 8.62 mM $HAuCl_4$ were dissolved in 3.75 mL ultrapure water under vigorous stirring at room temperature. The modified wafer was subsequently immersed in the mixed solution, and then 100 mM AA was added. The mixture was then allowed to react under static conditions at room temperature for 15 min. As-prepared R-CNAF was then washed with ethanol and dried in air. Finally, all of organics in the films were removed by electrochemical redox reaction to form fresh R-CNAF. Electrochemical redox reaction was performed on Chenhua 760 Electrochemical workstation at Cyclic voltammetry (CV) mode with scanning rate of 0.1 V/s and cycles of more than 300.

Characterization

XRD patterns were recorded on a Rigaku MiniFlex 600 powder diffractometer equipped with Cu Kα radiation (40 kV, 30 mA), at the rate of 0.2^o min^{-1} over the range $30\text{-}140^o$. SEM images were obtained using JEOL JSM-7900 with accelerating voltage of 5 kV and GBSH mode. TEM images were obtained using JEOL JEM-F200 TEM operated at 200 kV. Images were recorded on a Gatan OneView IS camera. The samples were scraped from the substrate and then sonicated in ethanol, next placed onto a carbon thin film on a Cu grid. The CD spectra were obtained on a JASCO J-1500 spectropolarimeter fitted with TCD and DRCD apparatus and data were collected with scanning rate of 20^o min^{-1} ranging from 190 nm to 800 nm with step of 0.1 nm at the temperature of 293 K.

Raman spectra were measured on a Renishaw Raman spectrometer using 514 nm laser with power of 20 mW. Parameters: 100-4000 cm^{-1}, step 0.2 cm^{-1}, integration time 10 s. In a typical SERS measurement on the R-CNAF with cylinder holes as the sample cells, 0.5 μL R-NAC aqueous solution with concentration of 4×10^{-2} M was injected into the cells and dried at room temperature, which gave loading amount of 2.5×10^{-8} mol/mm^2. Loading amount was calculated through $N = n/S$, in which N is the loading amount per unit area, *n* and *S* were the amounts of molecules added to the cell and the bottom area of the cells. N is an approximate value because the molecules adsorbed on the cylinder walls cannot be counted accurately.

Results and Discussion

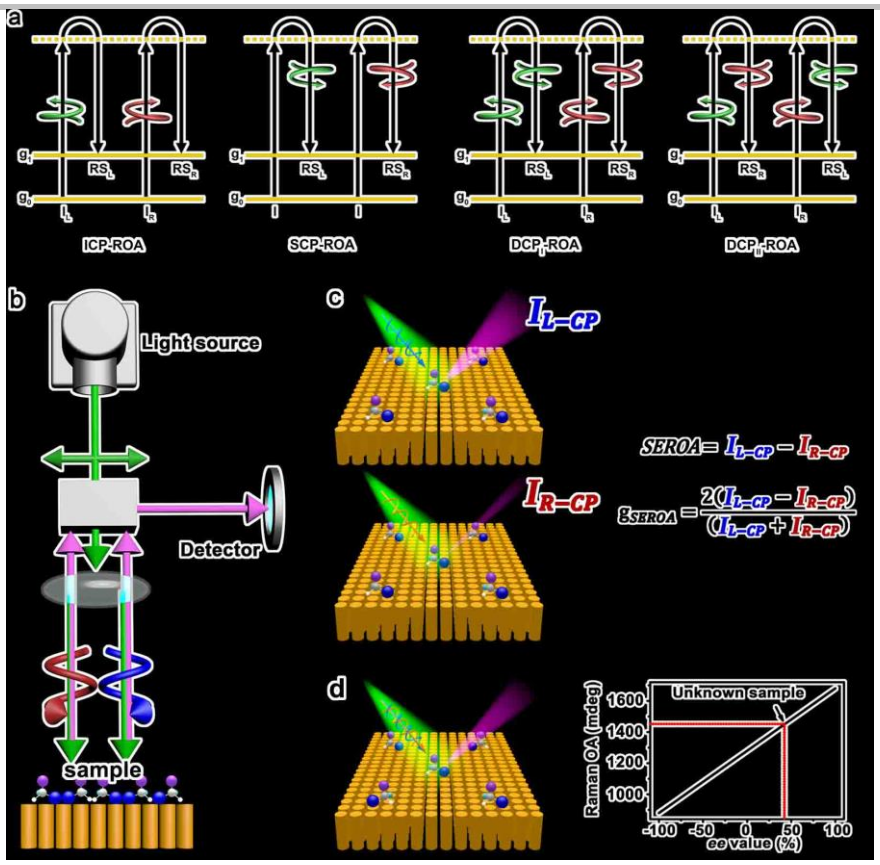

Figure S1. Schematic illustration of ROA and SEROA for discrimination of enantiomers. a, Energy-level diagrams of different ROA measurements illustrating the definition of ROA for a molecule undergoing a transition from the zeroth (g_0) to the first (g_1) vibrational level of the ground electronic state. b, ICP-SEROA, in which the chiral response originates from selective interaction between chiral molecules and incident left- and right-circularly polarized light on the nanostructured plasmonic surface. c, SEROA measurement of the same chiral molecules. d, The absolute configuration and *ee* values of unknown enantiomers can be obtained from SEROA standard curves. In b, c and d, green arrow: incident light. pink arrow: scattering light. blue helix: left polarized light. red helix: right polarized light.

SEROA, an extension of ROA to a wider range of molecules, is facilitated by coupling its structural sensitivity with the high sensitivity provided by plasmon resonance enhancement. Identical to ROA measurements, SEROA measurements can be divided into four modes: incident circular polarization (ICP), scattered circular polarization (SCP), in-phase dual circular polarization (DPC_I), and out-of-phase dual circular polarization (DCP_{II}) (Figure S1a). Figure S1b shows ICP-SEROA, in which the chiral response originates from selective interaction between chiral molecules and incident circularly polarized light on the nanostructured plasmonic surface. The SEROA and the *anisotropy* factor (*g*-factor) are common parameters for the degree of enantiomeric identification and are based on differential Raman scattering of left- and right-handed circularly polarized light incident ($I_{L\text{-}CP}$ and $I_{R\text{-}CP}$) on a chiral medium: SEROA=$I_{L\text{-}CP}$-$I_{R\text{-}CP}$; g_{SEROA} =2($I_{L\text{-}CP}$-$I_{R\text{-}CP}$)/($I_{L\text{-}CP}$+$I_{R\text{-}CP}$) (Figure S1c).

To detect and quantify enantiomers of an unknown compound (Figure S1d), (i) the composition and concentration should be detected by a certain method, such as SERS measurements on achiral nanostructured metal films; (ii) a SEROA standard working curve of the enantiomers should be established by comparing the SEROA intensity and *ee* values from -100% to +100% for known concentrations; (iii) the Raman OA intensity of an unknown compound can be obtained using an achiral plasmonic platform, and the *ee* values can be found from the SEROA standard curve. Similar to other OA-based spectroscopy methods (Table S1), SEROA cannot be used for racemates and is complicated and inaccurate because of weak interaction differences between the enantiomers and circularly polarized light or imperfect polarimeter systems.

Table S1. Chiral discrimination methods using polarized light. *

Methods	Characterization	Origin of phenomenon	Typical range
Optical Rotation (OR)	The angle between planes of emergent and incident linearly polarized electromagnetic waves.	Different velocities of left- and right-handed circularly polarized electromagnetic waves in medium.	Any
Electronic Circular Dichroism (ECD)	Absorption difference of oppositely circularly polarized electromagnetic waves.	Different absorptions of left- and right-handed circularly polarized electromagnetic waves due to the electronic transition or plasmonic resonance.	200~800 nm

Vibrational Circular Dichroism (VCD)	ECD with infrared light.	Different absorptions of left- and right-handed circularly polarized electromagnetic waves due to molecular vibration.	4500~750 cm^{-1}
Raman Optical Activity (ROA) ***SEROA (see Figure S1a)***	Differences in Raman scattering intensities corresponding to left- and right-handed circularly polarized electromagnetic waves based on incident circular polarization (ICP), scattered circular polarization (SCP), in-phase dual circular polarization (DPC_I) and out-of-phase dual circular polarization (DPC_{II}).	Different Raman scattering of left- and right-handed circularly polarized electromagnetic waves in medium due to molecular vibrations.	2000~100 cm^{-1}
X-ray Circular Dichroism (XCD)	The difference in extinction of incident oppositely circularly polarized X-rays.	Different absorptions of left- and right-handed circularly polarized X-ray in medium due to the inner electron transition.	100~10^5 eV
Circularly Polarization Luminescence (CPL)	The difference intensity of luminescent oppositely circularly polarized electromagnetic waves.	Different luminescence of left- and right-handed circularly polarized electromagnetic waves in medium due to transitions from electronic excited states.	200~800 nm

*Optical activity (OA) is the phenomenon of a chiral medium interacting differently with left- and right-handed circularly polarized electromagnetic waves. Depending on the mechanism of the interaction between materials and electromagnetic waves, OA can be employed in transmission (OR), UV-Vis absorbance (ECD), FTIR spectroscopy (VCD), Raman scattering (ROA), XAS (XCD), photoluminescence spectroscopy (CPL), and other methods. All of these methods and their extending applications originate from the chiral response of chiral materials/molecules to circularly polarized electromagnetic waves, resulting in the necessity of polarimetry systems and optical resonance during measurement. It is a challenging task to make the interactions between polarized electromagnetic waves and chiral matter sufficiently strong for practical applications. On the other hand, in commercial OA spectrometers, the polarization modulation method is commonly adopted to enhance sensitivity using a photoelastic modulator. During modulation, the polarization continuously changes from left-handed to right-handed circular polarization through linear polarization. The linear polarization component in a particular direction is involved in the polarization modulation at all times, which leads to the inaccuracy in circular polarization. The imperfect circularly polarization contains various artefacts. Furthermore, achieving absolute circular polarization at any wavelength is still a challenge.

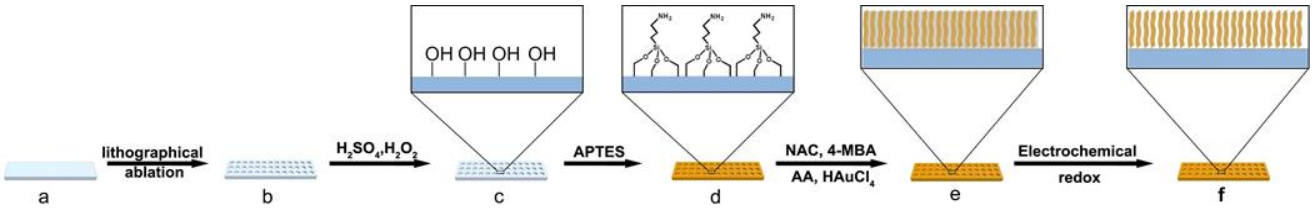

Figure S2. Synthesis of CNAFs. a, Silicon-based wafer for CNAF growth. b, The wafer was lithographically ablated with cylinder holes with a diameter of 1 mm and a depth of 1 mm. c, The wafer was activated with a H_2SO_4/H_2O_2 mixed solution to generate multiple silanol groups on the surface. d, The amino groups were chemically modified on the surface *via* condensation between the silanol groups and the siloxane of APTES. e, As-prepared CNAFs were grown on the wafer surface by introducing a synthesis gel containing $HAuCl_4$, AA, MBA and S/R-NAC. f, Pure inorganic CNAFs were obtained by electrochemistry.

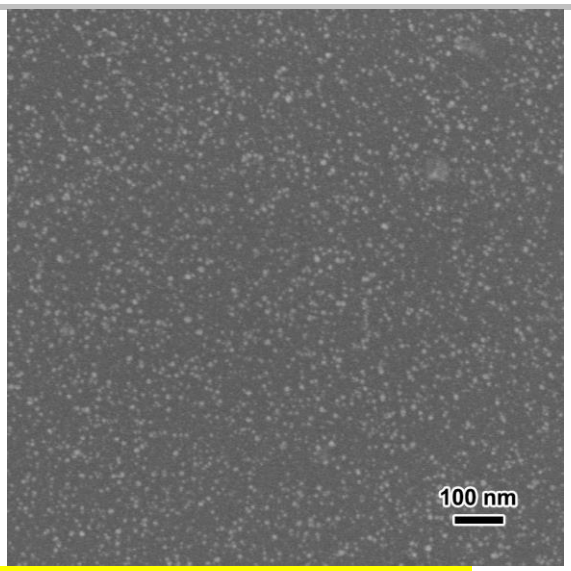

Figure S3. SEM image of Au seeds grown on Silica wafer. The diameters of the seeds were 3~5 nm.

The seed mediated growth process of CNAFs was supposed to be the following steps: (i) Au^{3+} were absorbed to the activated substrate through the formation of Au-NH_2. (ii) Au seeds formed in situ on the substrate by reducing Au^{3+} to Au^{+}/Au^{0} with the exist of AA. At the same time, Au^{3+} interact with -SH of NAC to generate complex precursor in the solution. (iii) The precursor goes on to be reduced at the interface between Au seeds and the substrate. During this stage, because of chiral steric hindrance effect from NAC, the reduced Au^{+}/Au^{0} arranged in a defined chiral direction. (iv) With Au^{+}/Au^{0} constantly reduced at the interface between grown gold domain and the substrate, chiral Au fibre vertically grew on the substrate.

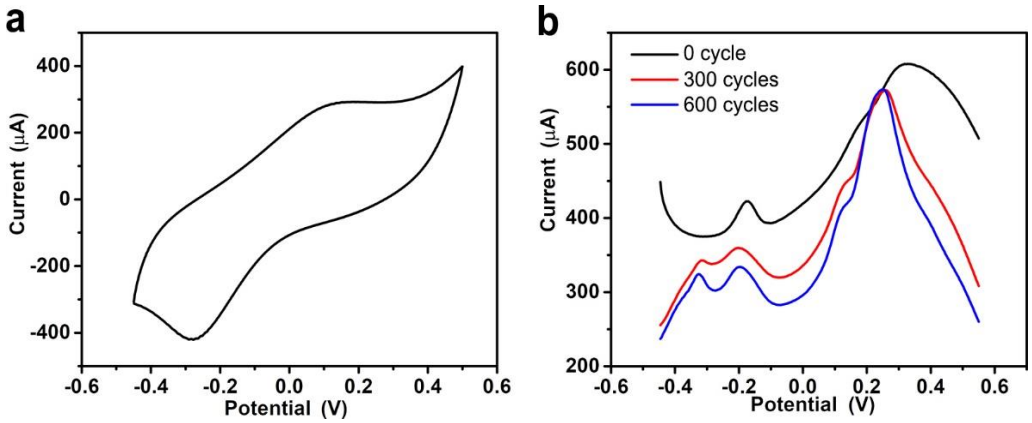

Figure S4. Electrochemical removal of organic molecules in the CNAFs. a, Cyclic voltammetry (CV) curve of CNAFs. b, Differential pulse voltammetry (DPV) curve of CNAFs before and after 300 and 600 cycles. CV and DPV curves were recorded in the range of -0.45 to 0.55 V with a scan rate of 0.1 V s^{-1}. After 300-600 cycles, the DPV peak positions and intensities remained stable, indicating that the electrochemical redox reaction was complete and the organics were fully removed.

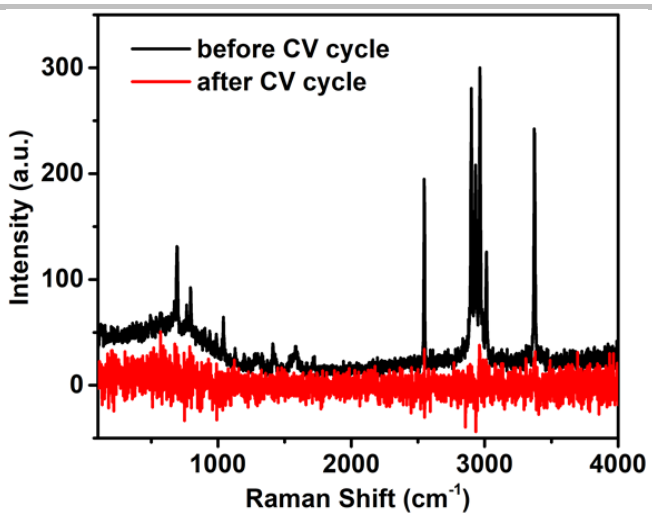

Figure S5. Raman spectra of R-CNAFs before and after electrochemical treatment. Before the treatment, obvious Raman shifts corresponding to NAC were observed. After the treatment, these characteristic peaks disappeared, indicating that the organic molecules were removed completely. Raman shifts at 688, 803, 1576, 2541, 2889, 2956, 3012, and 3371 cm^{-1} correspond to N-H bending, S-H bending, C=O bending, S-H stretching, symmetric C-H stretching, asymmetric C-H stretching, asymmetric C-H stretching and symmetric N-H stretching, respectively.[1]

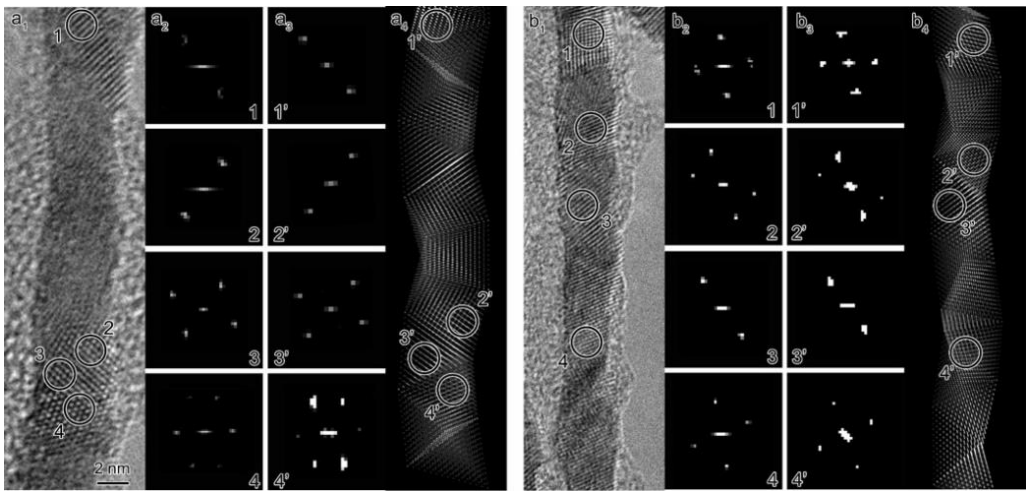

Figure S6. Imperfect *tetrahelix* of R-CNAF. a_1, a_2, b_1, b_2 HRTEM image and corresponding FDs of an Au fiber with imperfect BCB structure. a_3, a_4, b_3, b_4, Simulated TEM image and FDs of ideal BCB structure showing partial correspondence with the observed images. This simulation was calculated by eMap[2] with the resolution of 3.33 Å. For simulation, the thickness was set to be 200~500, step 10 and defocus was -100~100, step 10.

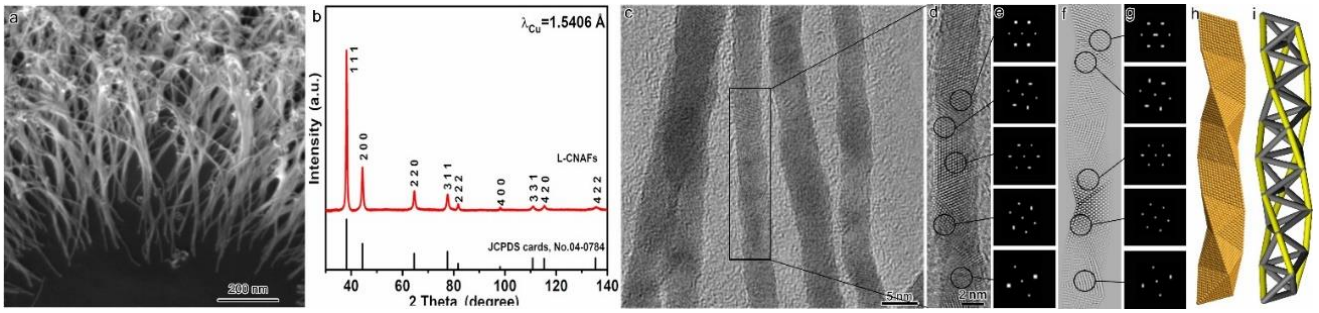

Figure S7. Characterizations of L-CNAF. a, SEM image of Au fibers vertically grown on Si wafer. b, XRD pattern exhibits *fcc* structure of Au with preferred crystal growth along the <111> direction. c, High magnification TEM image of Au nanofibers, showing polycrystalline structure. d, e, HRTEM image and corresponding FDs of an Au fibre with ideal BCB structure. f, g, Simulated TEM image and FDs of left-handed BCB structure showing good correspondence with the observed images. h, Schematic drawing of a left-handed chiral Au fibre, showing the BCB helix configuration from multiply twinned tetrahedral Au nanocrystals with a face-sharing relationship. i, A triple helix is revealed by connecting edge outside (yellow line). The synthetic chemical molar composition of L-CNAF was R-NAC: 4-MBA: $HAuCl_4$: AA = 15:8:25:40.

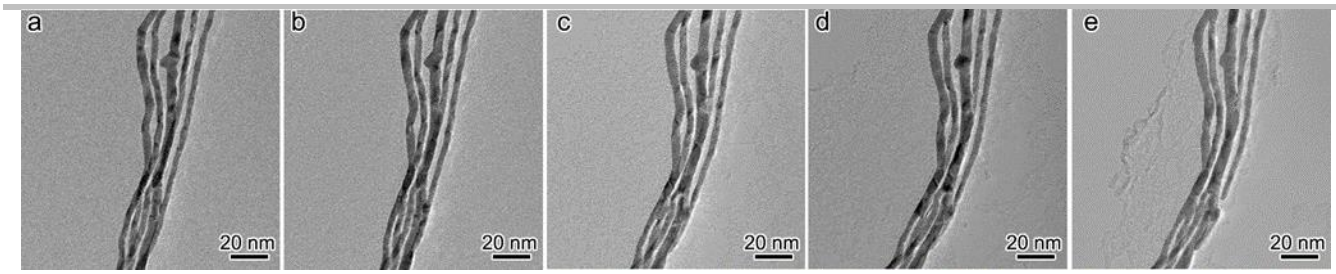

Figure S8. TEM images of Au fibres at the same position under electron beam irradiation at different periods. a, 0 min. b, 10 min. c, 20 min. d, 25 min. e, 30 min. The carbon film on the copper mesh shrank around the fibre under the irradiation of the electron beam, indicating that the shadowed area around the fibre consisted of shrunk carbon film rather than organics after electrochemical treatment.

Table S2. SERS-ChA effect of CNAFs for one hundred enantiomers presenting different electric dipole configurations, sizes, chromophores, concentrations, and *ee* values (listed in order of decreasing *g*-factor).

No.	Enantiomer	Structure	Molar mass	Spectra	Linearity	*g*-factor
1	(S)/(R)-1,2,3,4-Tetrahydro-1-naphthylamine	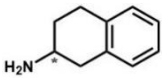	147.22	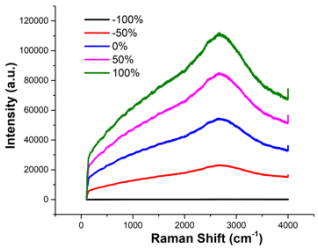	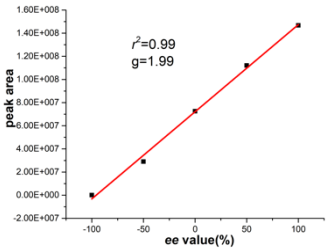	1.99
2	L/D-Glutamine	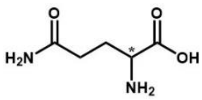	146.14	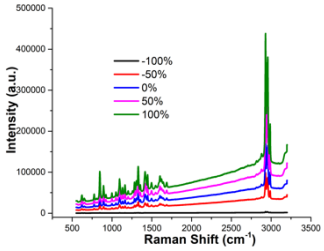	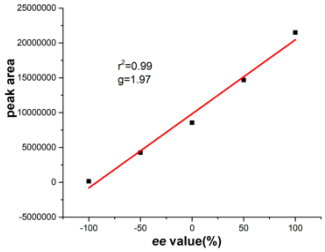	1.97
3	L/D-Methionine	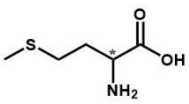	149.21	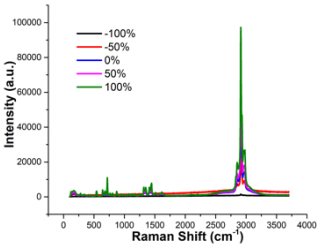	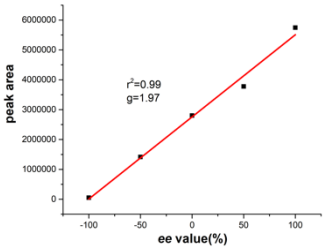	1.97
4	L/D-Phenylglycine	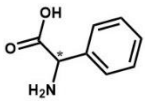	151.16	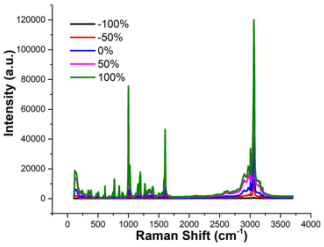	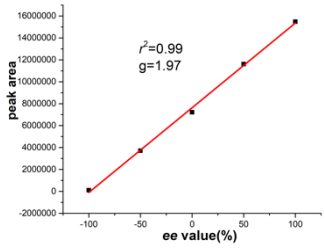	1.97

5	(1S,2S)/(1R,2R)-1,2-Diaminocyclohexane	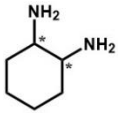	114.19	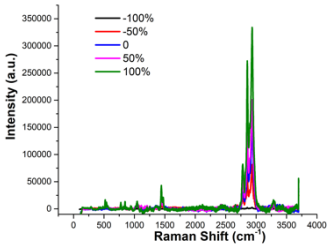	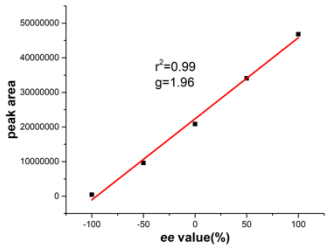	1.96
6	(S)/(R)-2-Amino-3-methyl-1-butanol	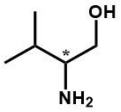	103.16	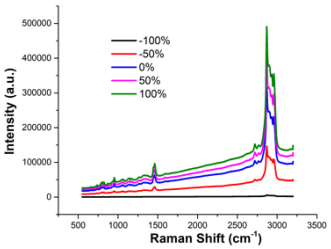	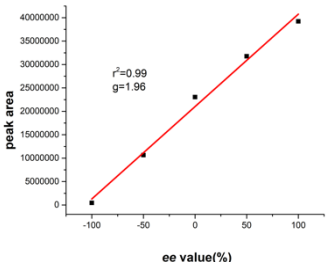	1.96
7	L/D-Leucinol	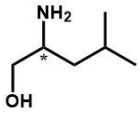	117.19	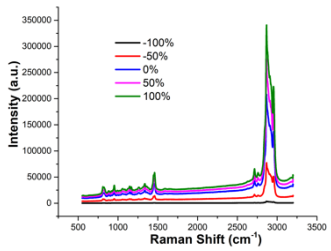	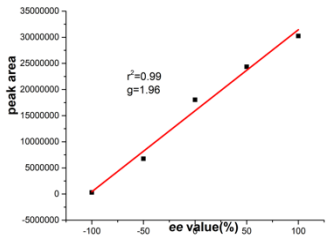	1.96
8	Methyl (S)/(R)-lactate	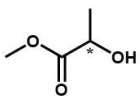	104.10	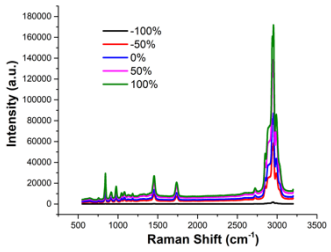	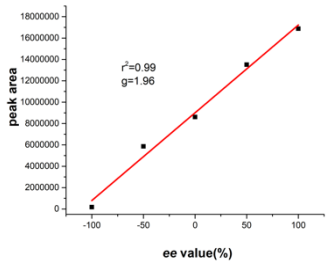	1.96
9	(+)/(-)Troger's base	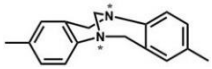	250.34	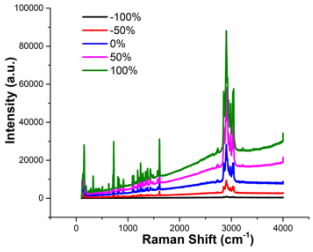	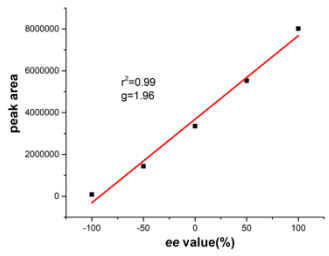	1.96
10	(S)/(R)-Phenylglycinamide	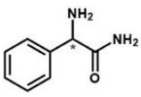	150.18	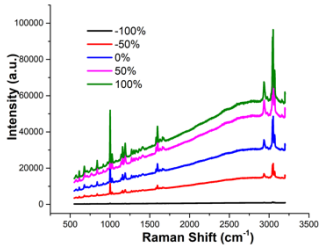	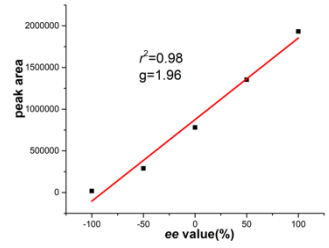	1.96

11	L/D-Carnitine	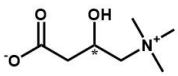	161.20	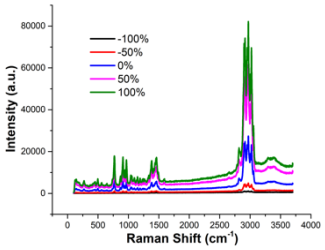	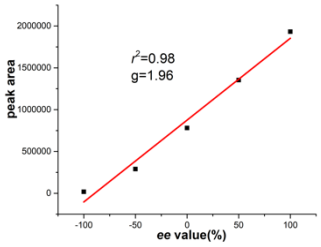	1.96
12	L/D-Asparagine	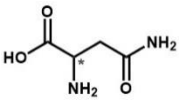	132.12	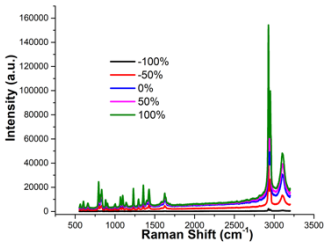	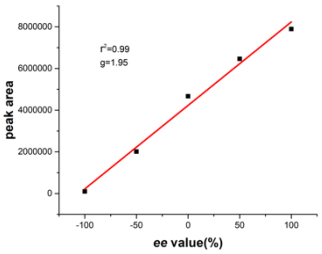	1.95
13	L/D-tert-Leucine	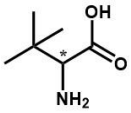	131.17	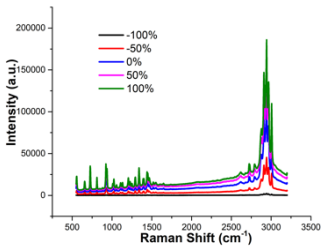	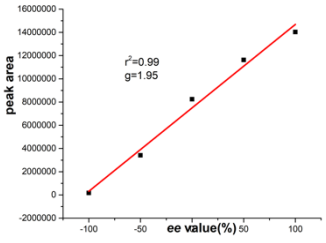	1.95
14	(S)/(R)-3-Amino-1,2-propanediol	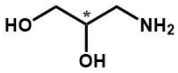	91.11	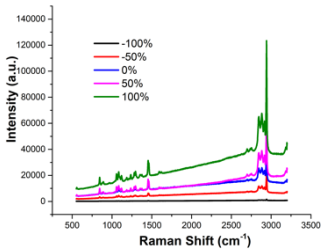	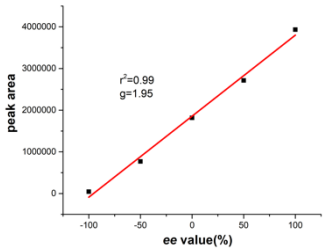	1.95
15	(S,S)/(R,R)-Benzenemethanamine	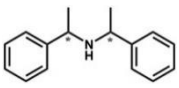	225.33	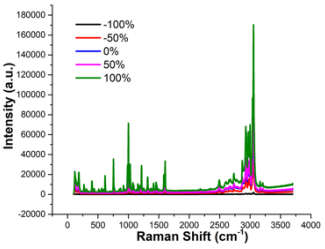	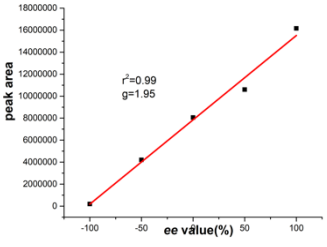	1.95
16	L/D-Threonine	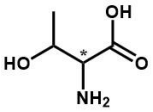	119.12	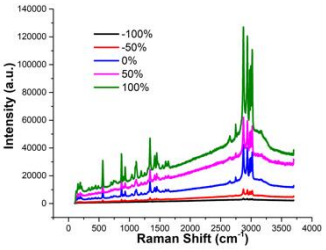	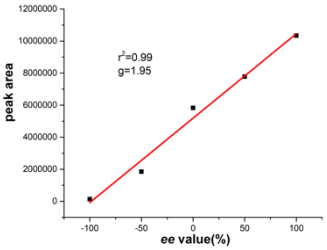	1.95

17	L/D-Arginine	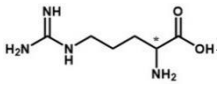	174.20	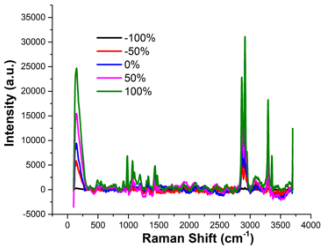	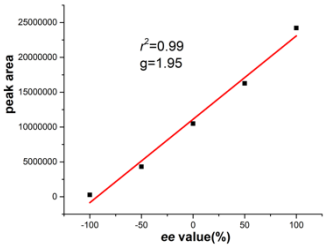	1.95
18	L/D-Mannitol	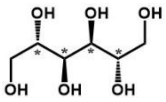	182.17	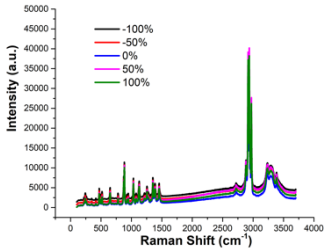	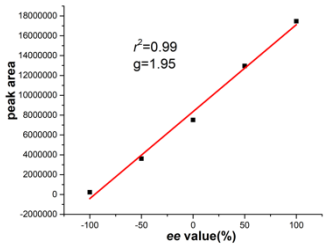	1.95
19	(S)/(R)-N, α-Dimethylbenzylamine	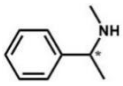	135.21	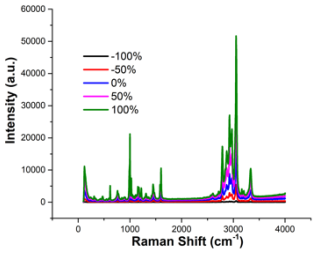	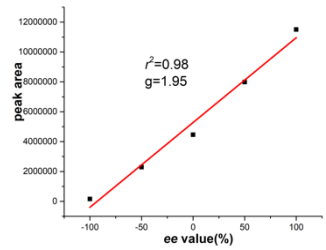	1.95
20	(S)/(R)-1-Phenylethylamine	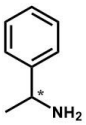	121.18	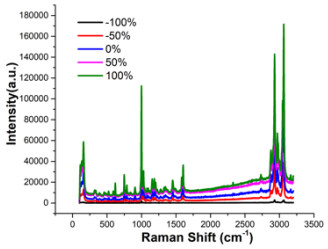	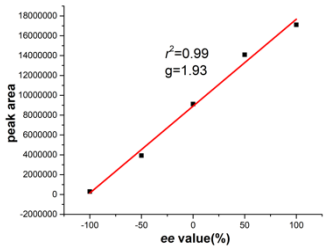	1.93
21	(S)/(R)-3-Amino-3-phenylpropan-1-ol	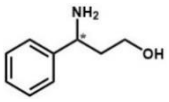	151.21	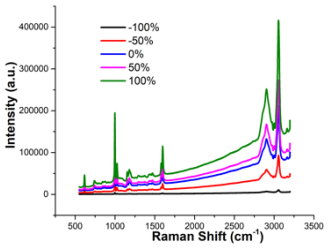	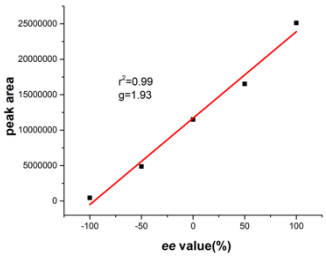	1.93
22	(S)/(R)-Limonene	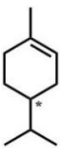	138.25	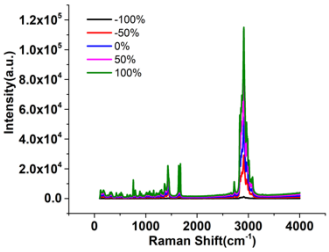	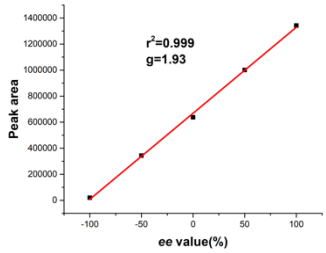	1.93

23	(S)/(R)-2-Amino-1-propanol	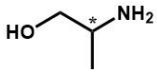	75.11	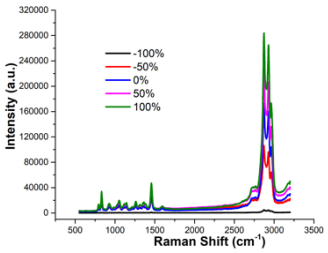	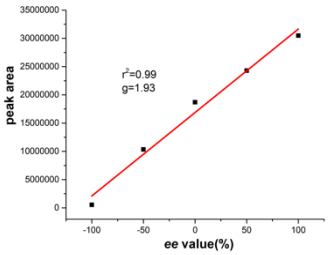	1.93
24	(2S,3S)/(2R,3R)-Dihydroxybutane-1,4-dioic acid diethyl ester	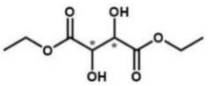	206.19	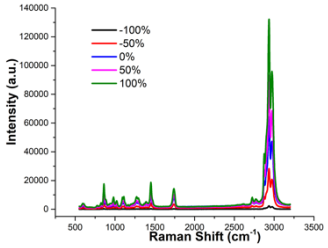	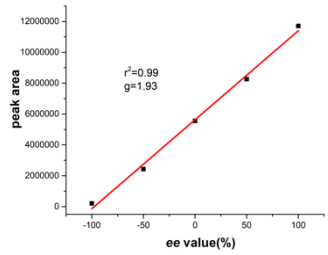	1.93
25	(S)/(R)-1-Aminoindane hydrochloride	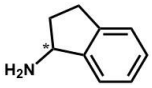	133.19	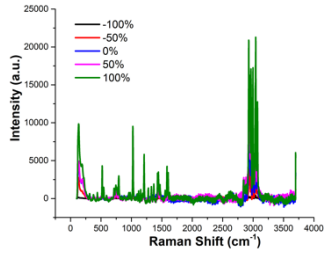	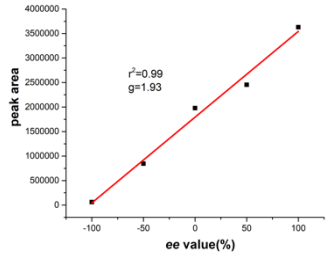	1.93
26	L/D-Alanine	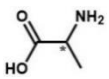	89.09	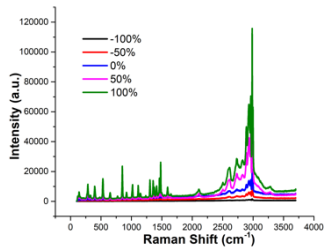	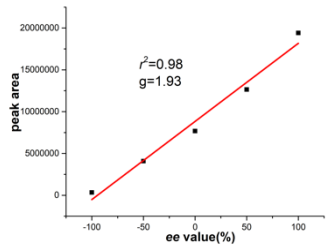	1.93
27	N-Acetyl-L/D-cysteine	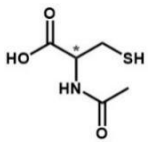	163.19	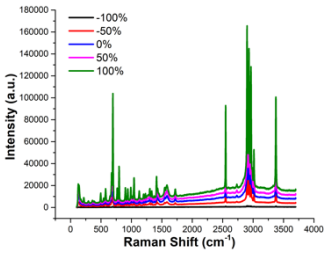	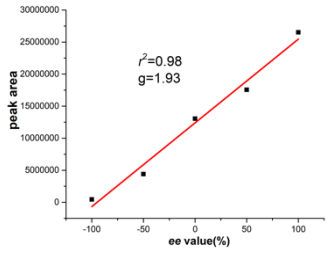	1.93
28	(S, S)/(R, R)-Bis(α-methylbenzyl)amine hydrochloride	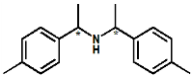	253.38	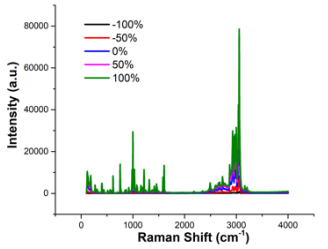	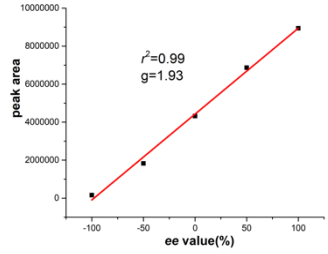	1.93

29	L/D-Iditol	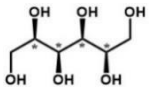	182.17	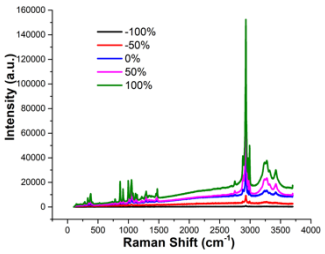	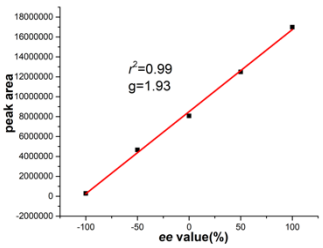	1.93
30	L/D-Cyclohexylglycine	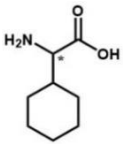	157.21	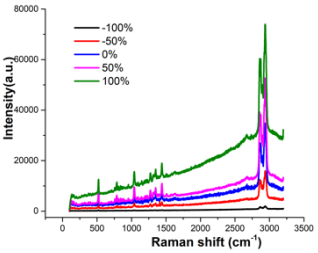	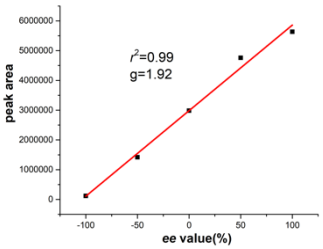	1.92
31	(S)/(R)-2-Chloropropionic acid	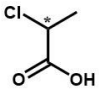	108.52	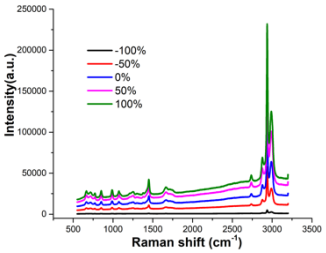	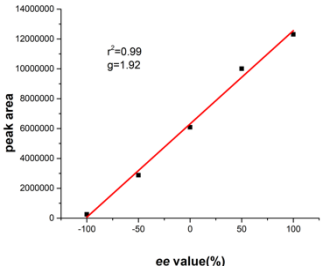	1.92
32	L/D-Valine	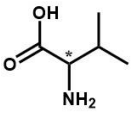	117.15	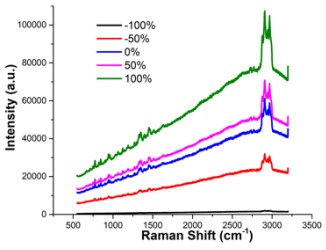	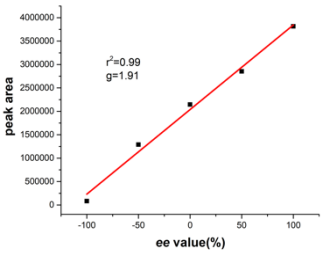	1.91
33	L/D-Phenylglycinol	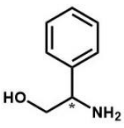	137.18	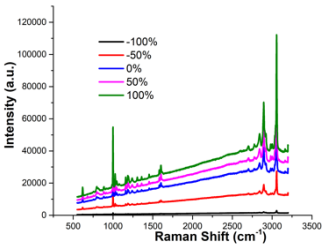	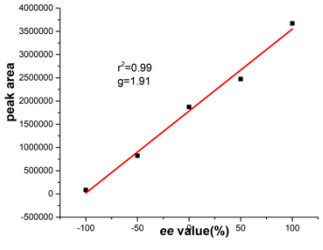	1.91
34	(S)/(R)-1-(4-Pyridyl)ethanol	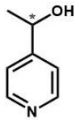	123.15	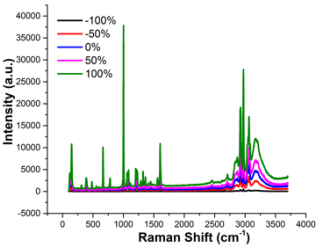	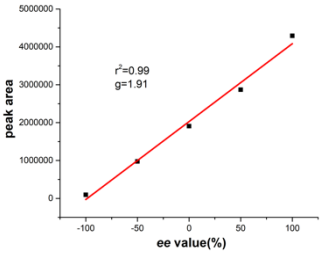	1.91

35	(S)/(R)-Glycidyl butyrate	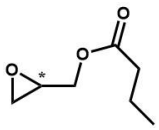	144.17	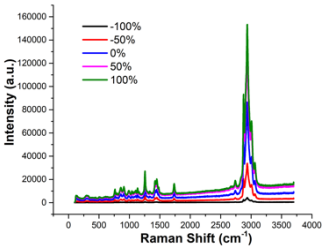	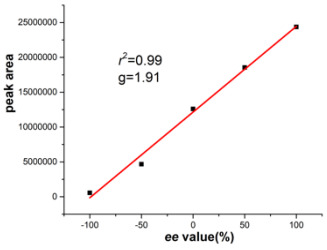	1.91
36	(S)/(R)-1,2-Butanediol	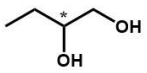	90.12	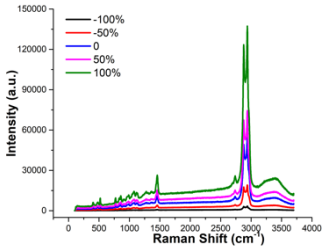	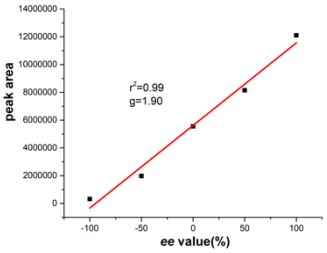	1.90
37	(S)/(R)-2,2,2-Trifluoro-1-(9-anthryl)ethanol	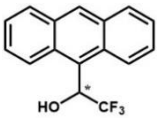	276.25	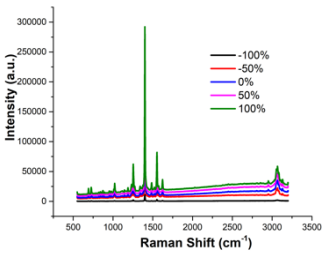	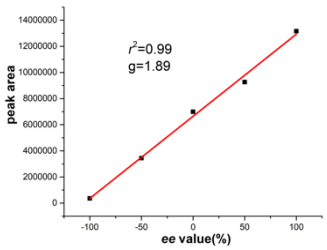	1.89
38	L/D-Glutamic acid	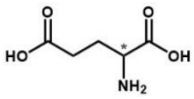	147.13	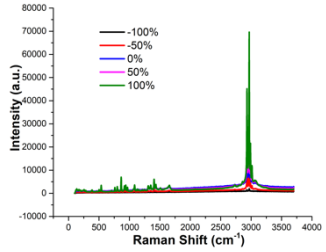	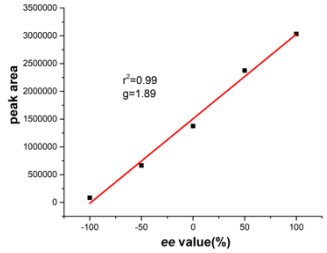	1.89
39	(S)/(R)-Epichlorohydrin	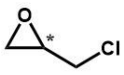	92.52	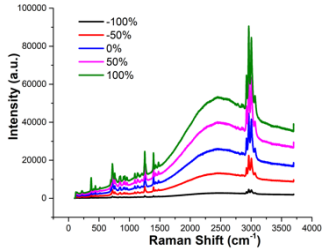	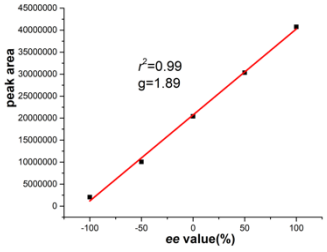	1.89
40	L/D-Pipecolinic acid	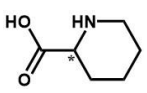	129.16	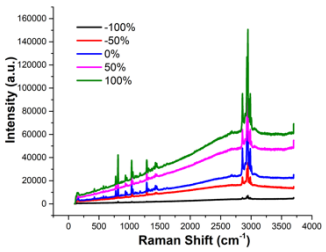	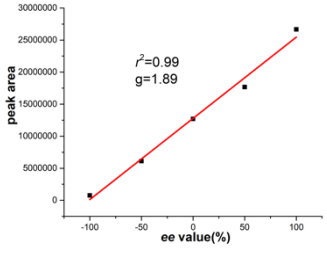	1.89

41	(S)/(R)-Benzoin	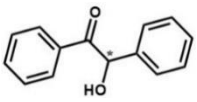	212.24	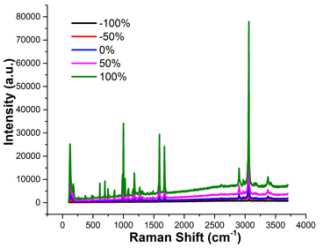	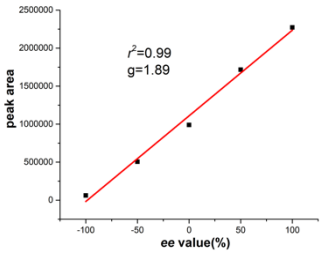	1.89
42	(S)/(R)-(Camphorylsulfonyl)oxaziridine	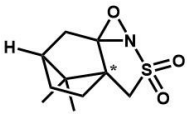	229.3	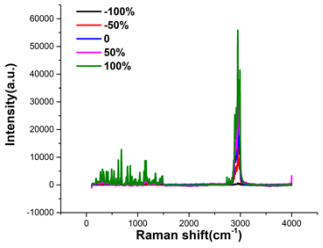	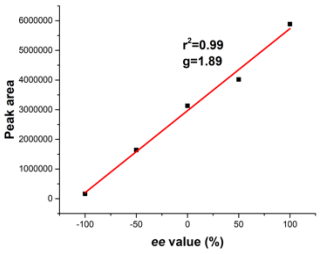	1.89
43	L/D-Tyrosine	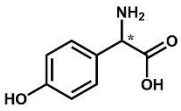	181.19	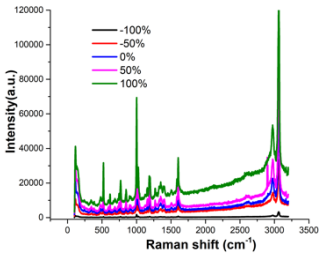	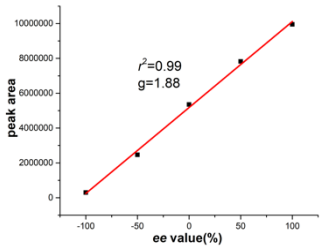	1.88
44	(S)/(R)-1-Phenylethanol		122.16	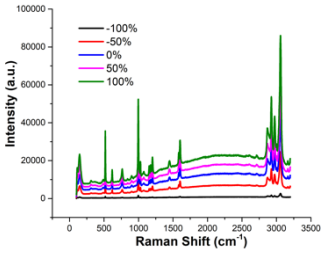	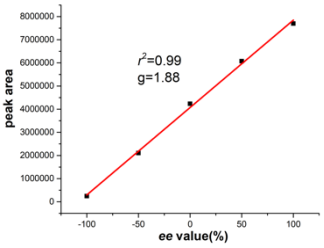	1.88
45	(S)/(R)-2-Chloromandelic acid	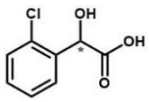	186.59	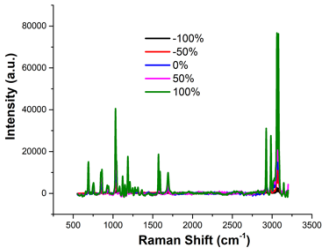	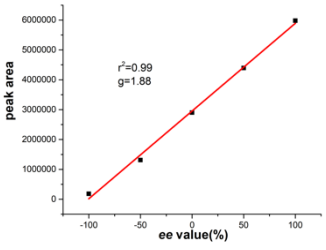	1.88
46	(S)/(R)-10-Camphorsulfonic acid	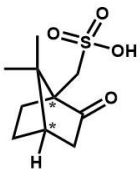	232.30	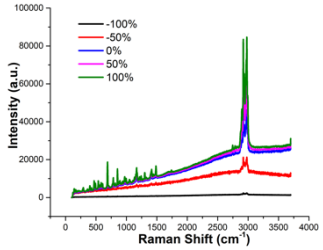	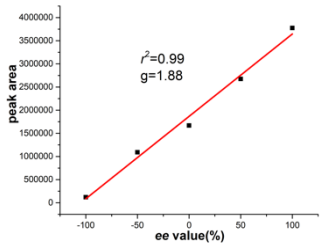	1.88

47	L/D-Phenylalanine	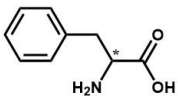	165.19	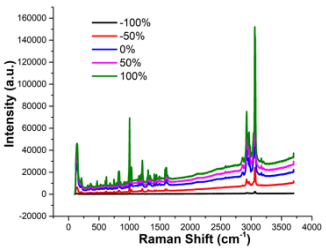	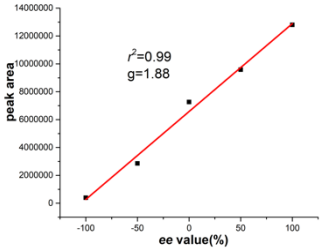	1.88
48	L/D-Malic Acid	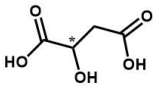	134.09	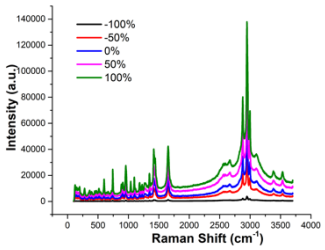	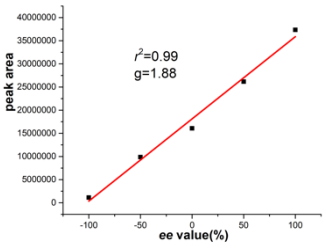	1.88
49	(S)/(R)-α,α-Diphenyl-2-pyrrolidine methanol	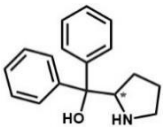	253.34	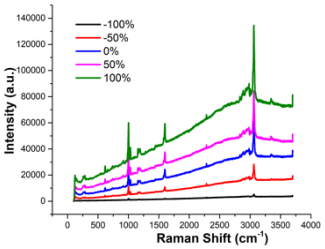	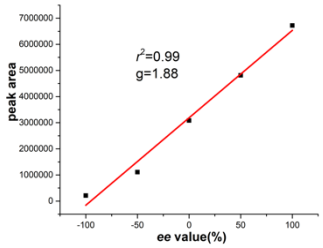	1.88
50	(S)/(R)-1,2-Epoxybutane	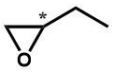	72.11	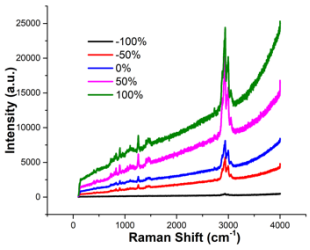	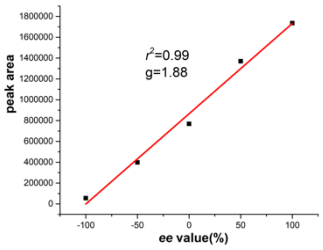	1.88
51	(S)/(R)-Glycidol	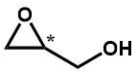	74.08	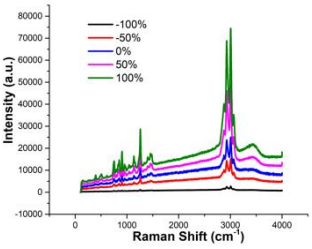	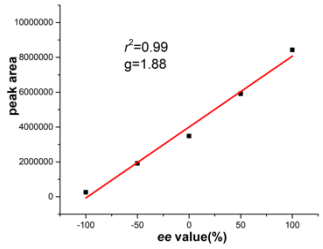	1.88
52	L/D-Glyceraldehyde	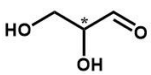	90.08	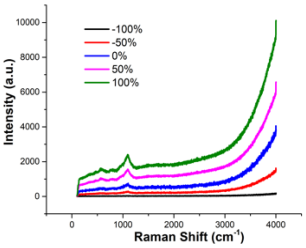	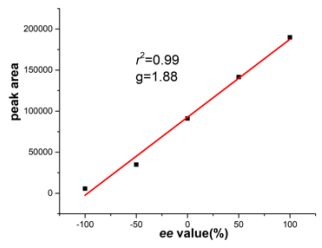	1.88

53	(S)/(R)-2-Butanol	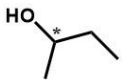	74.12	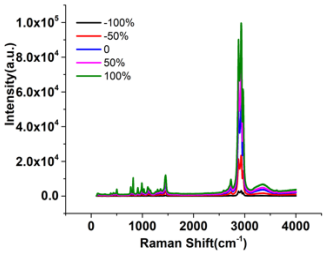	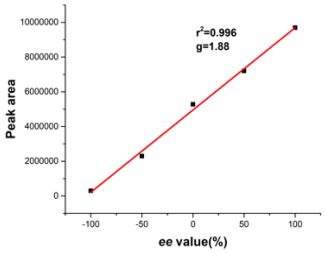	1.88
54	(S)/(R)-Methyl mandelate	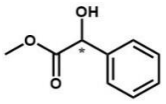	166.17	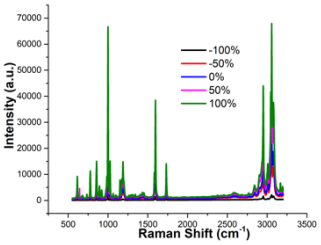	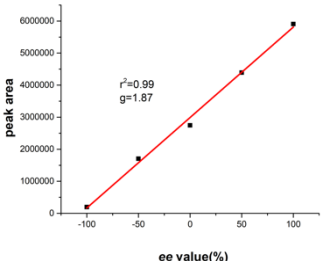	1.87
55	L/D-Phenyllactic acid	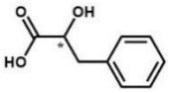	166.17	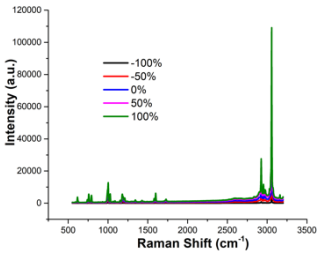	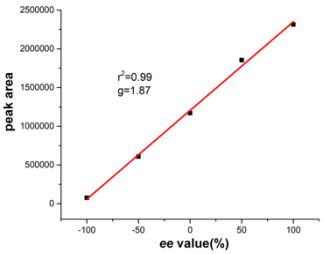	1.87
56	L/D-Histidine	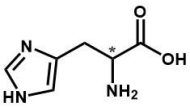	155.15	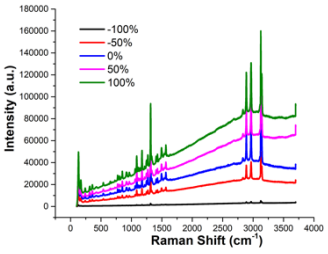	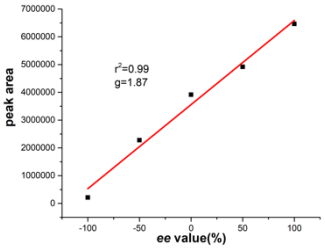	1.87
57	L/D-Cysteine	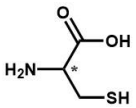	121.16	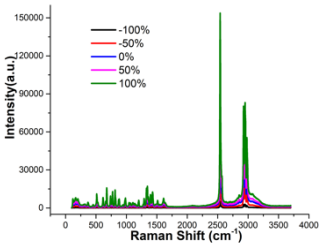	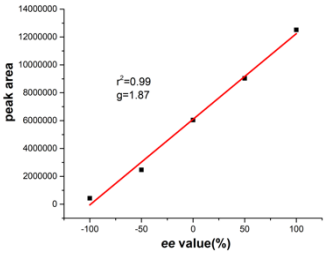	1.87
58	L/D-Prolinamide	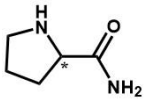	114.15	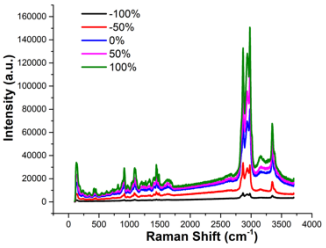	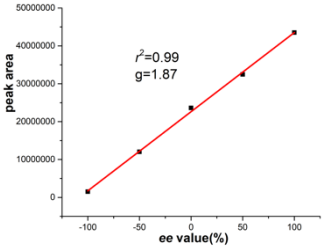	1.87

59	(S)/(R)-2-Phenylpropionic acid	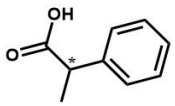	150.17	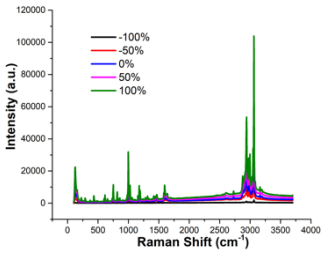	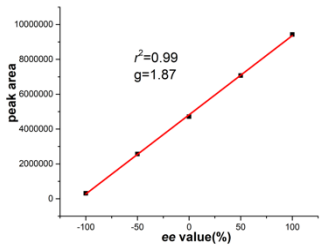	1.87
60	L/D-Tryptophan	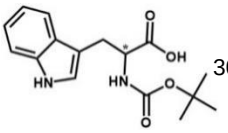	304.34	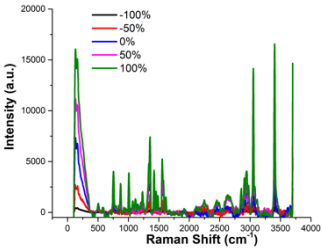	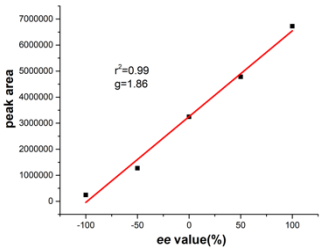	1.86
61	L/D-Mandelic acid	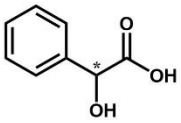	152.15	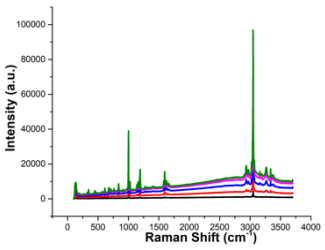	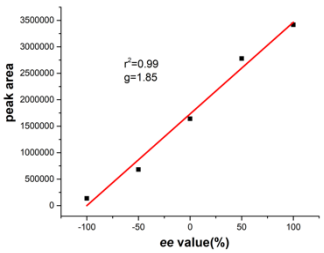	1.85
62	(S)/(R) - Methoxyphenylacetic acid	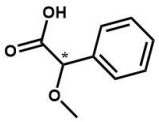	166.17	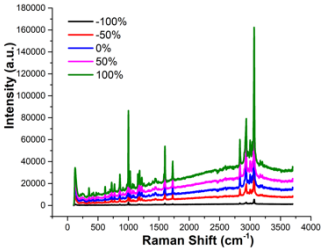	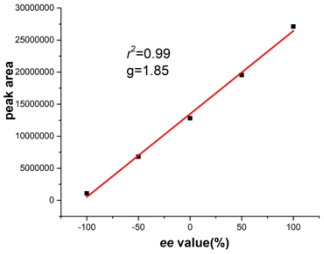	1.85
63	(S)/(R)- 2-Amino-1,1,1-trifluoropropane hydrochloride	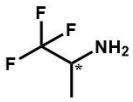	113.08	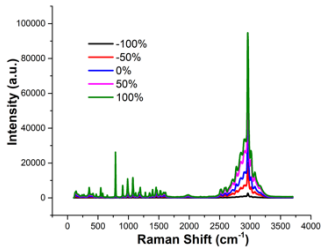	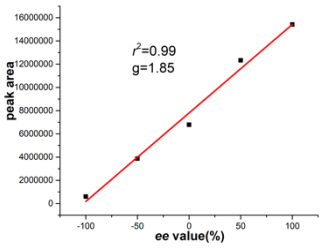	1.85
64	(S)/(R)-Thalidomide	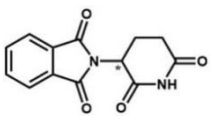	258.23	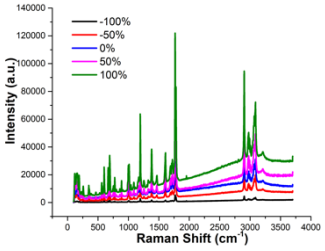	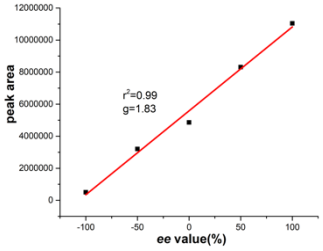	1.83

65	L/D-Lysine	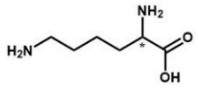	146.19	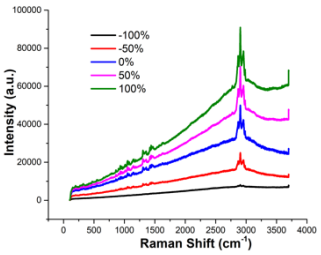	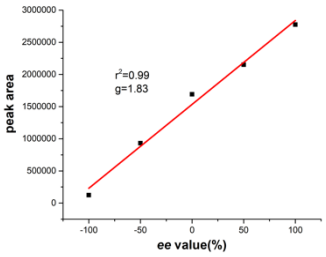	1.83
66	(1S,2S)/(1R,2R)-N,N-Dimethylcyclohexane-1,2-diamine	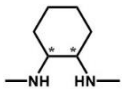	142.24	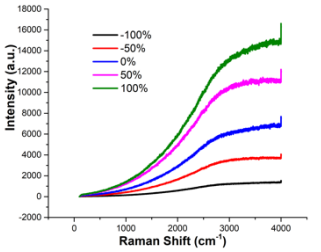	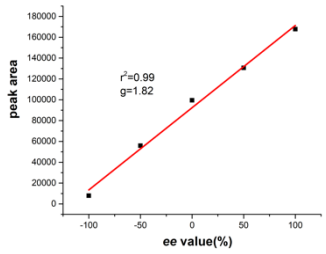	1.82
67	2,2-Dimethyl-α,α,α',α'-tetra(1-naphthyl)-1,3-dioxolane-4,5-dimethanol	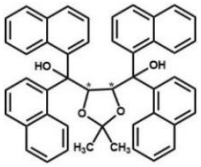	666.8	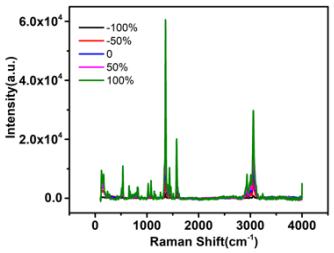	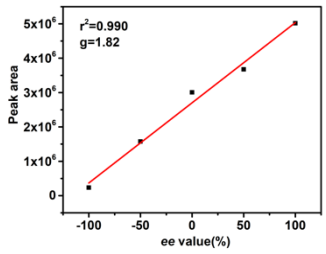	1.82
68	L/D-Glucose	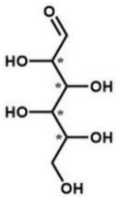	180.16	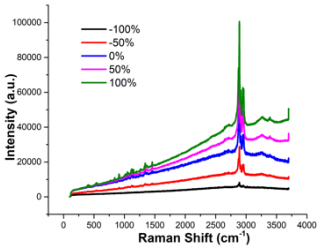	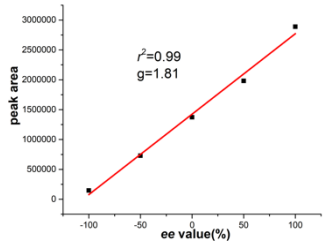	1.81
69	L/D-Talitol	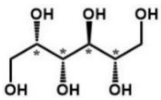	182.17	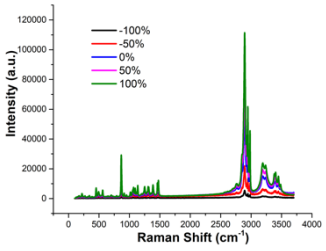	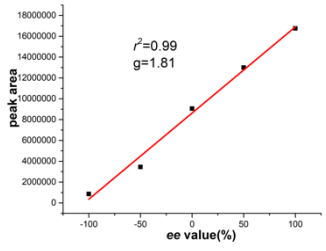	1.81
70	(S)/(R)-1-Phenyl-1,2-ethanediol	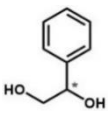	138.16	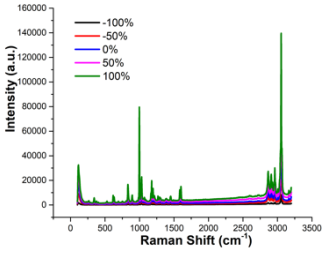	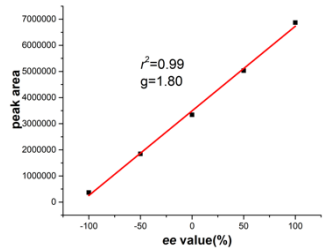	1.80

71	Boc-L/D-Tyr-OH	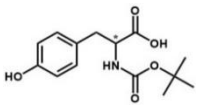	281.30	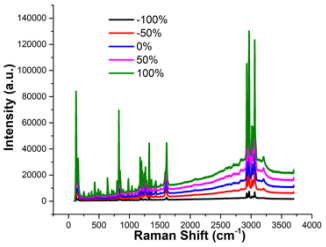	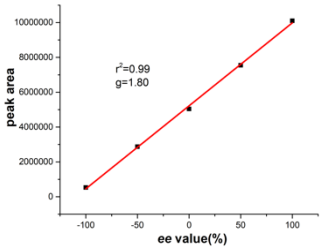	1.80
72	(S)/(R)-1-(2-Pyrrolidinylmethyl)pyrrolidine	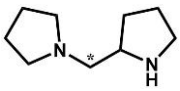	154.25	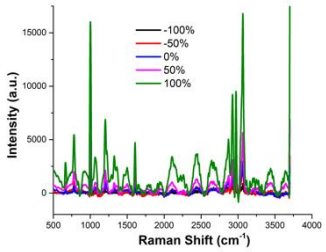	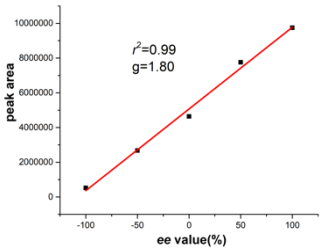	1.80
73	(1S,2S)/(1R,2R)-1,2-Diphenylethylenediamine	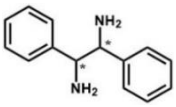	212.29	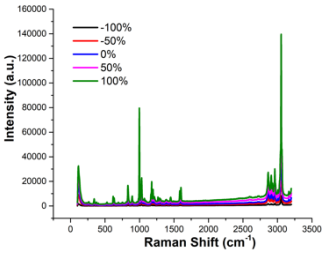	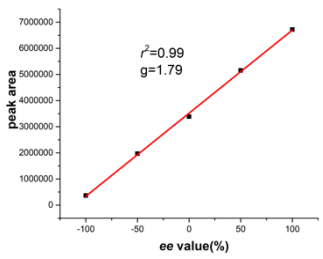	1.79
74	L/D-Penicillamine	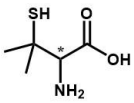	149.21	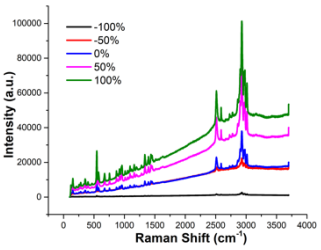	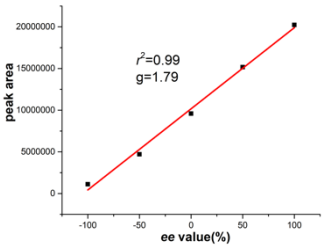	1.79
75	(S)/(R)-1,2-Propanediol carbonate	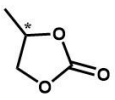	102.09	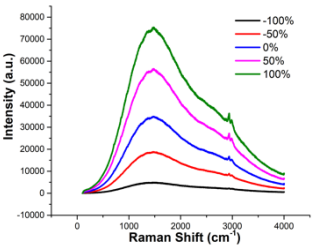	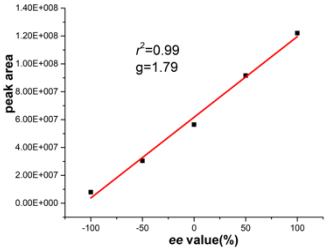	1.79
76	(S)/(R)-1,2-Propanediol	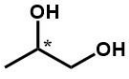	76.09	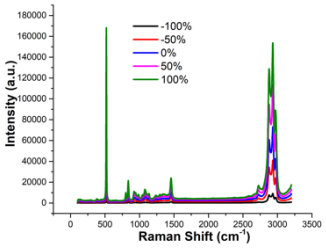	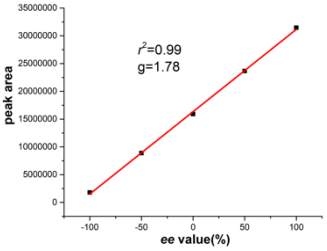	1.78

77	L/D-Phenylalaninol	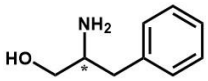	151.21	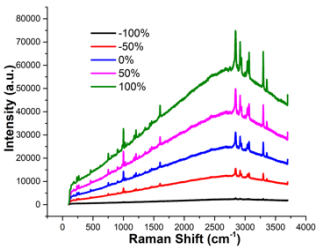	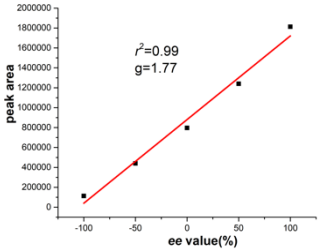	1.77
78	L/D-Serine	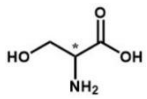	105.09	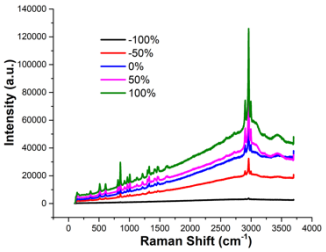	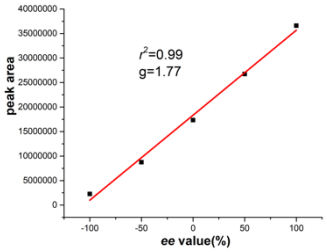	1.77
79	L/D-Sorbitol	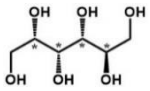	182.17	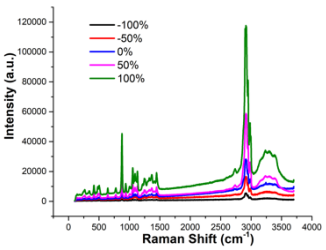	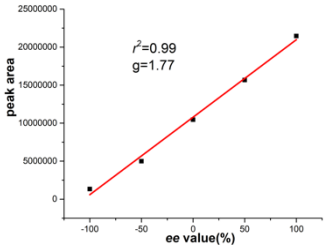	1.77
80	L/D-tyrosinol	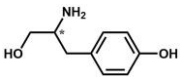	167.21	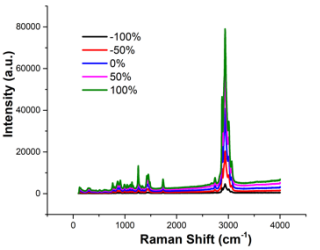	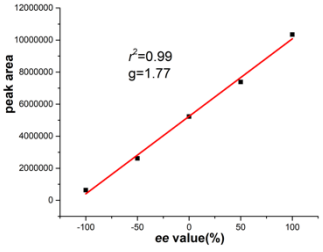	1.77
81	L/D-Tartaric acid	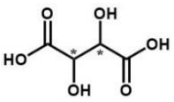	150.09	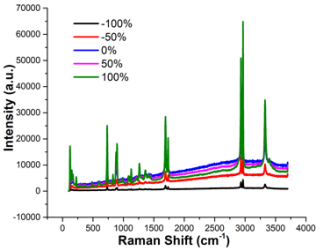	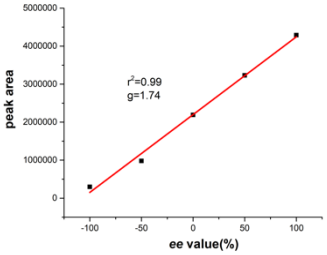	1.74
82	N-carbobenzoxy-L/D-leucine	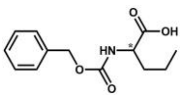	265.30	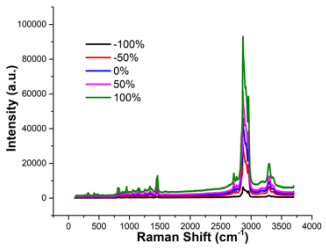	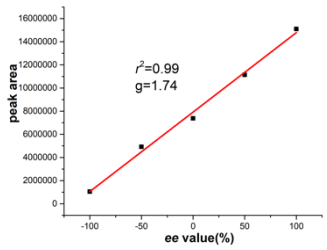	1.74

83	L/D-2-Amino-4-methylpentanoic acid	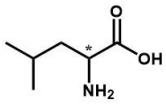	131.17	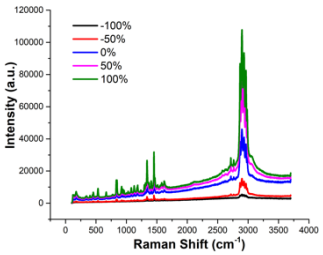	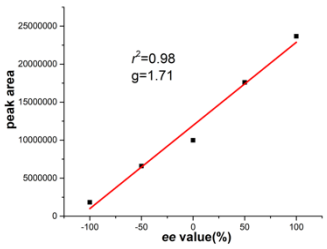	1.71
84	Trans/cis-stilbene oxide	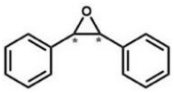	196.24	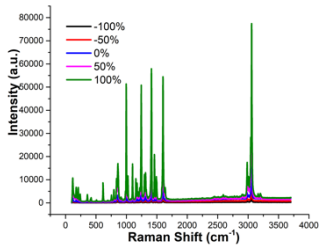	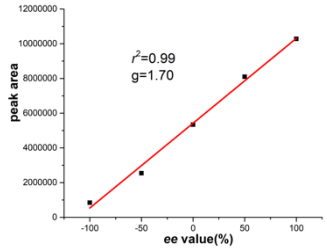	1.70
85	(S)/(R)-2-(Methoxymethyl)pyrrolidine	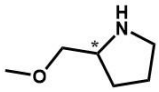	115.17	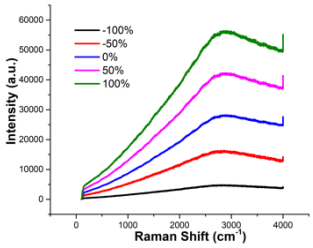	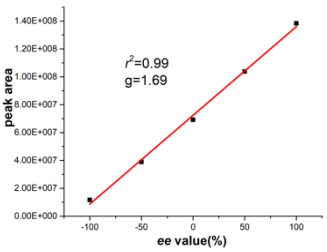	1.69
86	(S)/(R)-1,1'-Bi-2-naphthol	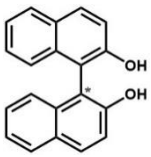	286.32	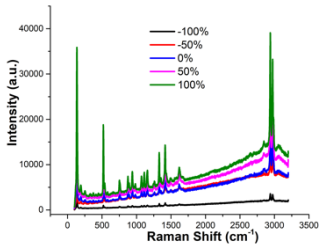	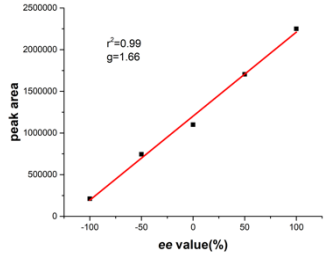	1.66
87	L/D-Cystine	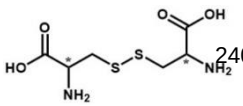	240.30	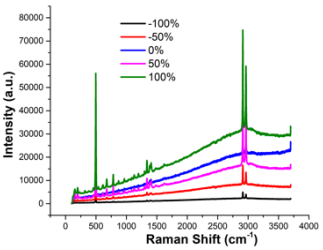	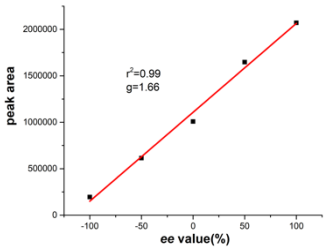	1.66
88	(S)/(R)-3-Chloro-1,2-propanediol	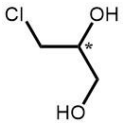	110.54	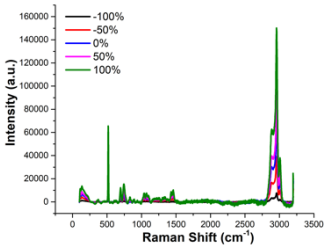	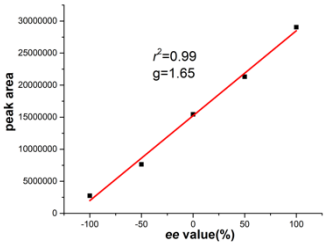	1.65

89	(S)/(R)-1,2,3,4-Tetrahydro-1-naphthol	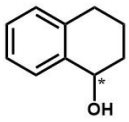	148.20	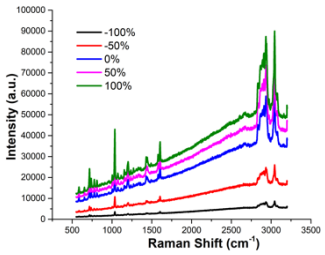	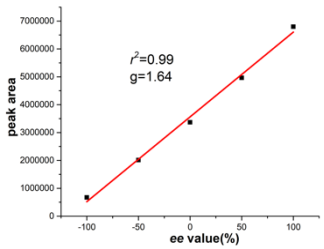	1.64
90	L/D-Pyroglutamic acid	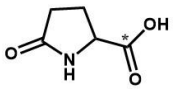	129.11	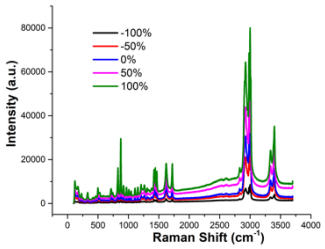	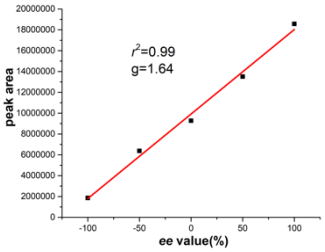	1.64
91	(S)/(R)-N-Benzyl-1-phenylethylamine	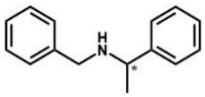	211.30	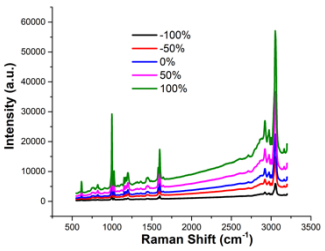	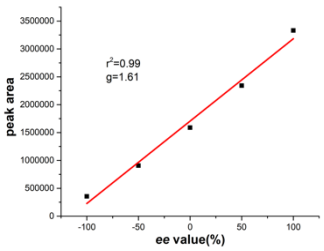	1.61
92	L/D-Aspartic acid	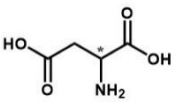	133.10	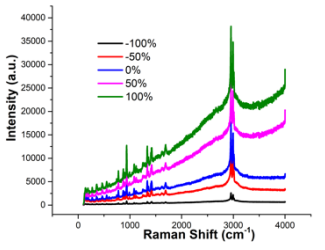	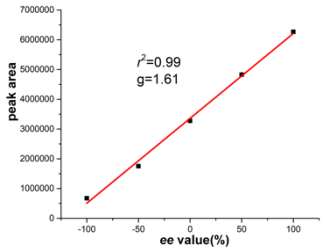	1.61
93	L/D-Prolinol	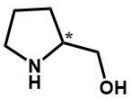	101.15	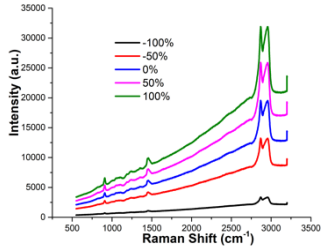	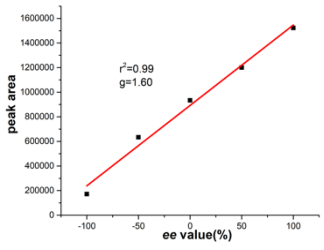	1.60
94	(S)/(R)-1-(1-Naphthyl)ethylamine	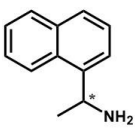	171.24	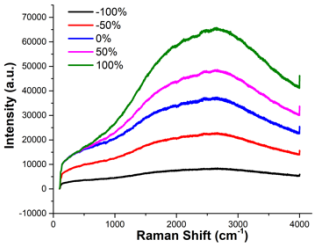	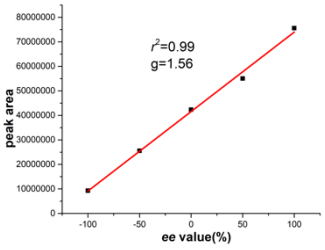	1.56

95	(1S,2S)/(1R,2R)-N,N'-Dimethyl-1,2-cyclohexanediamine	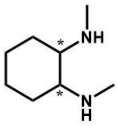	142.24	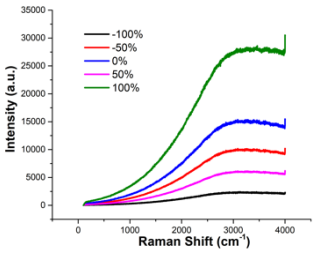	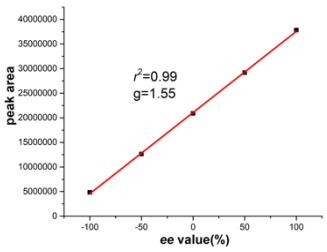	1.55
96	(2S,3S)/(2R,3R)-2-Amino-3-methylpentanoic acid	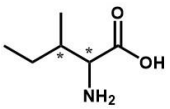	131.17	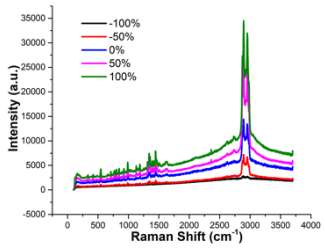	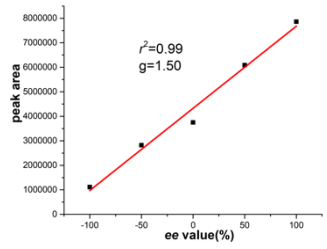	1.50
97	L/D-Proline	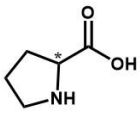	115.13	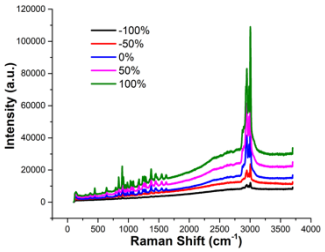	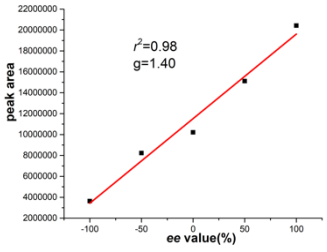	1.40
98	L/D-Carvone	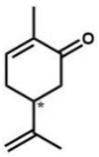	150.22	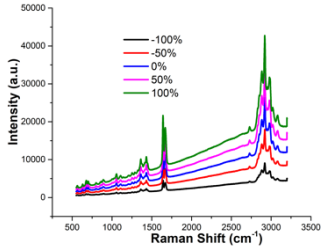	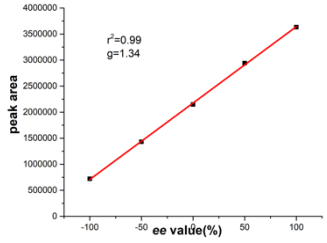	1.34
99	(1S,2R)/(1R,2S)-1-Amino-2-indanol	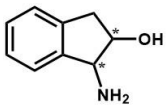	149.19	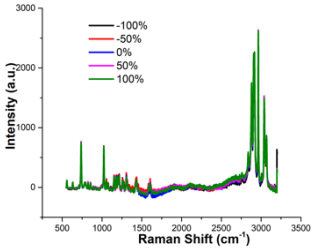	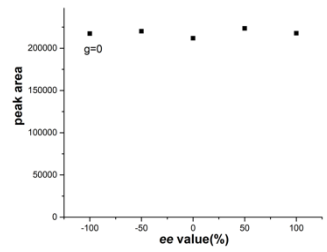	0
100	(1S,2R)/(1R,2S)-2-Amino-1,2-diphenylethanol	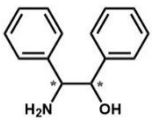	213.28	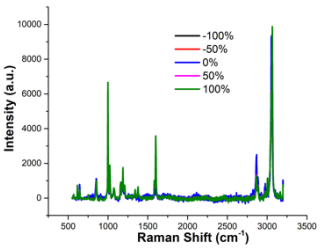	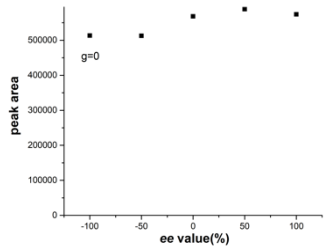	0

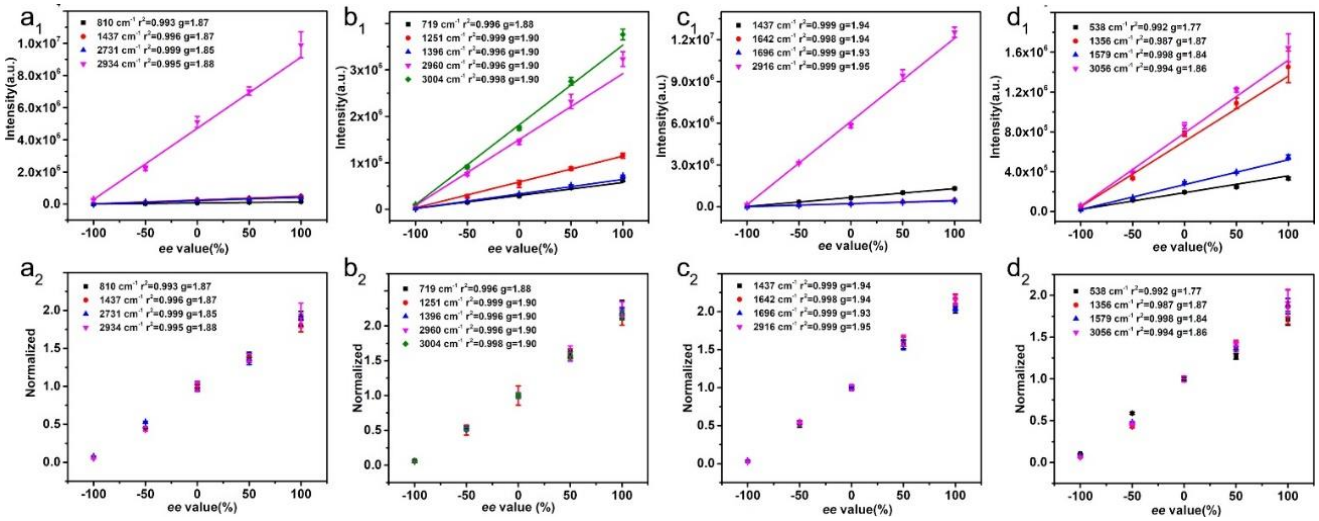

Figure S9. SERS-ChA of different Raman scattering peaks for one molecule. Absolute (a_1-d_1) and area normalized linear correlations of characteristic Raman peak areas of enantiomers (a_2-d_2) with *ee* values of 2-butanol ($a_{1\text{-}2}$), epichlorohydrin ($b_{1\text{-}2}$), Limonene ($c_{1\text{-}2}$), and DTNDD ($d_{1\text{-}2}$). As for 2-butanol, Raman shifts at 810, 1437, 2731, and 2934 cm^{-1} correspond to (C_2)C-O stretching, CH_2 scissoring/CH_3 asymmetric scissoring, and combination and CH_3 symmetric scissoring, respectively. For epichlorohydrin, Raman shifts at 719, 1251, 1396, 2960 and 3004 cm^{-1} correspond to C-Cl stretching, ring breathing, *gauche*-2 and cis, CH_2(Cl) and *gauche*-2, respectively. For limonene, Raman shifts at 1437, 1642, 1696 and 2916 cm^{-1} correspond to CH_2 scissoring, C=C stretching, C-H stretching and C-H stretching. [3] There is no reference of DTNDD.

Raman intensities ($I^{ee}_{normalized,Ramanshift}$) were normalized using the formula $I^{ee}_{normalized,Ramanshift} = I^{ee}_{Ramanshift} / I^{0\%}_{Ramanshift}$, in which $I^{ee}_{Ramanshift}$ is the Raman intensity of the samples with nonzero *ee* values and $I^{0\%}_{Ramanshift}$ is the Raman intensity of the sample with an *ee* value of 0%. The intensities of the characteristic Raman shifts were quite different because the Raman activity of each vibration mode was different. However, the same linear correlations were acquired by ruling out the impact of Raman activity, because the same trend was observed between *ee* value and Raman intensity at different characteristic Raman shifts. The similarity of linear correlations between normalized Raman intensity and the *ee* value provides an effective route for detecting and quantifying an unknown enantiomeric compound by establishing a working curve of any identified characteristic Raman peak.

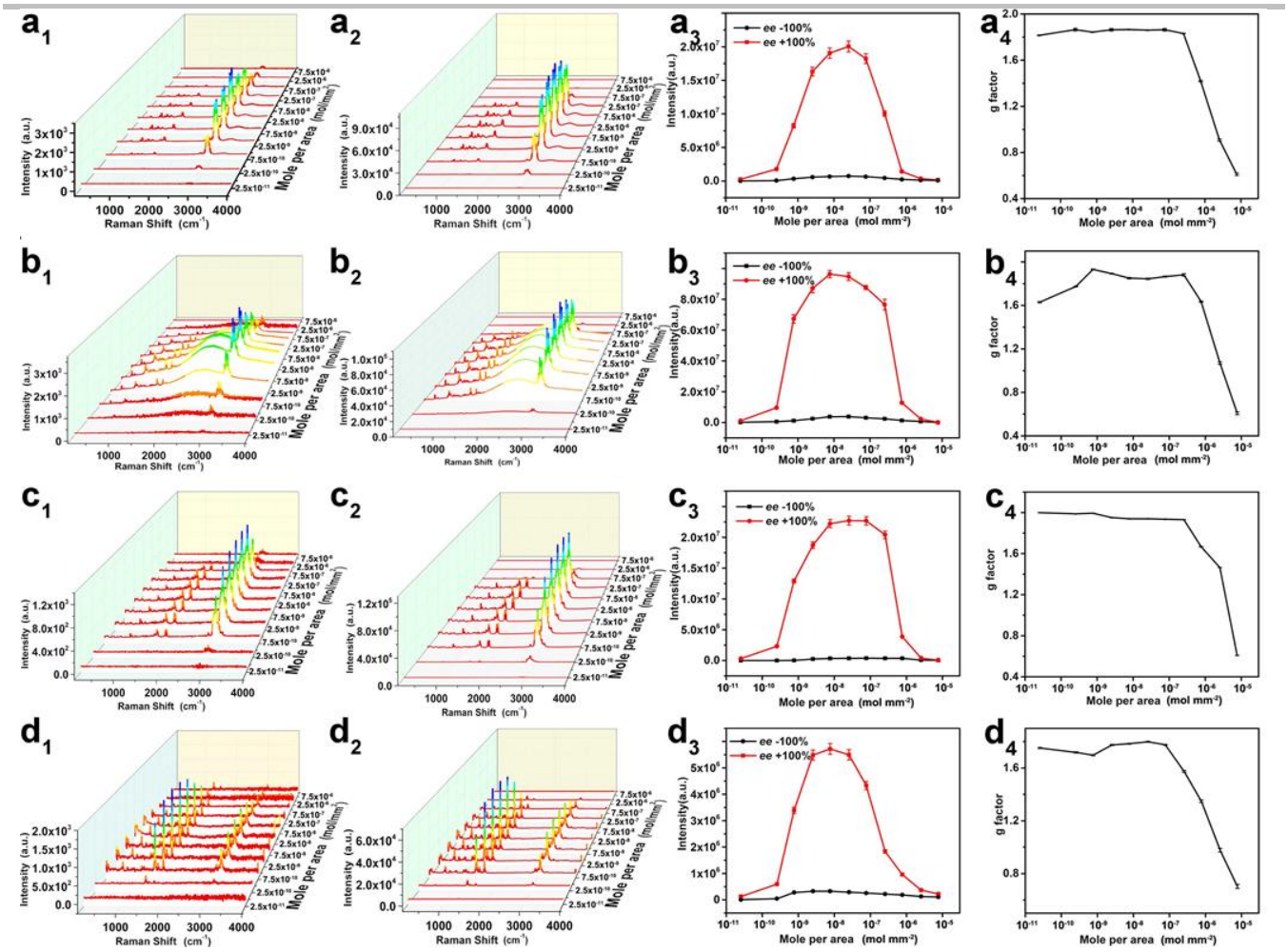

Figure S10. SERS-ChA effect at different concentrations of four enantiomers on R-CNAF. Raman spectra of S- (*ee*=100%) and R-enantiomers (*ee*=-100%), the largest peak areas, and *g*-factors at loading amounts of 2.5×10^{-11}, 2.5×10^{-10}, 7.5×10^{-10}, 2.5×10^{-9}, 7.5×10^{-9}, 2.5×10^{-8}, 7.5×10^{-8}, 2.5×10^{-7}, 7.5×10^{-7}, 2.5×10^{-6}, and 7.5×10^{-6} mol/mm^2 on R-CNAFs. a, 2-Butanol (MW:74.1). b, Epichlorohydrin (MW: 92.5). c, Limonene (MW:136.2). d, DTNDD (MW:666.8). Decreases in the SERS intensity at low and high concentrations would result from inadequate loading amounts and the presence of excess molecules outside the CNAFs. Fluctuations in *g*-factor at low concentrations would arise from weak SERS intensity, and decreases in *g*-factor at high concentrations would also be caused by the presence of excess molecules outside the CNAFs.

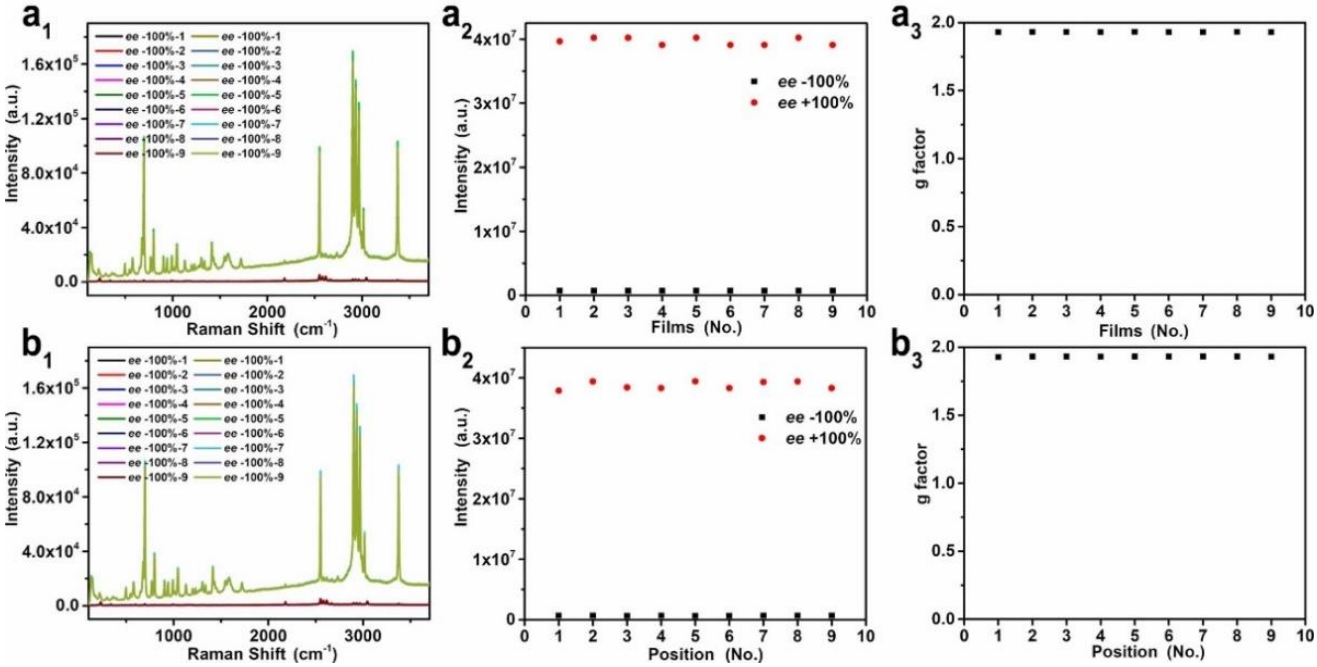

Figure S11. Repeatability of the SERS-ChA effect of CNAFs using different sample cells. a, SERS-ChA measurements for nine different R-CNAFs using S/R-NAC (shown as *ee* values of -100% and 100%) as test molecule: Raman spectra of S/R-NAC (a_1) intensity at a Raman shift of 2930 cm^{-1} (a_2) and *g*-factor (a_3). The error in the *g*-factor between R-CNAFs was 0.1%, indicating the consistency of the CNAFs fabricated using the same preparation parameters. b, SERS-ChA measurements for nine different cylinders in one plate using S/R-NAC (shown as *ee* values of -100% and 100%) as the test molecule: Raman spectra of S/R-NAC (b_1), intensity at a Raman shift of 2930 cm^{-1} (b_2) and *g*-factor (b_3). The error in the *g*-factor between cylinder cells was 0.2%, indicating the uniformity of CNAFs and ensuring the accuracy of the SERS-ChA.

Table S3. Raman intensities and *g* factors of NAC with *ee* value of -100% and 100% at 2930 cm^{-1} measured at nine different R-CNAFs.

Film No.	-100%	+100%	*g*-factor
1	7.12×10^5	3.97×10^7	1.9295
2	7.08×10^5	4.02×10^7	1.9308
3	7.05×10^5	4.02×10^7	1.9311
4	7.01×10^5	3.91×10^7	1.9295
5	7.02×10^5	4.02×10^7	1.9313
6	7.00×10^5	3.91×10^7	1.9297
7	7.01×10^5	3.91×10^7	1.9296
8	7.02×10^5	4.02×10^7	1.9314
9	6.99×10^5	3.91×10^7	1.9298

Table S4. Raman intensities and *g* factors of NAC with *ee* value of -100% and 100% at 2930 cm^{-1} measured at nine different cylinders on the same R-CNAFs.

Cylinder No.	-100%	+100%	*g*-factor
1	6.97×10^5	3.79×10^7	1.9277
2	6.94×10^5	3.94×10^7	1.9308
3	6.80×10^5	3.84×10^7	1.9304
4	6.87×10^5	3.83×10^7	1.9295
5	6.78×10^5	3.94×10^7	1.9323
6	6.76×10^5	3.83×10^7	1.9307
7	6.87×10^5	3.93×10^7	1.9313
8	6.88×10^5	3.94×10^7	1.9314
9	6.85×10^5	3.83×10^7	1.9298

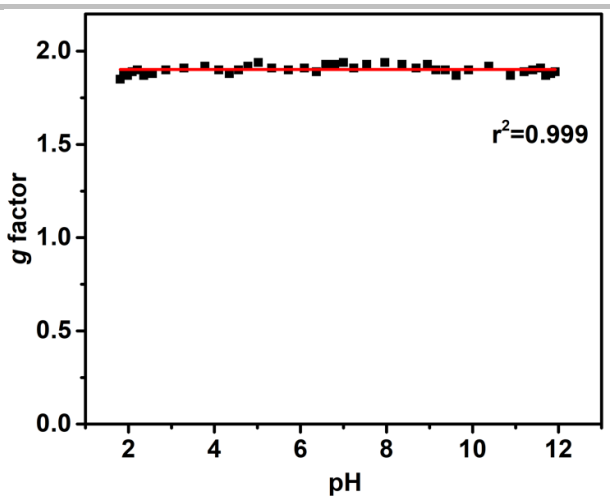

Figure S12. Stability of CNAF in strong acid, alkali and salt conditions. To investigate the stability of CNAF, R-CNAF was first put in Britton-Robison (BR) buffer with pH ranging from 1.81 to 11.92 for 2 hours, following washing with ethanol and dried in air before use. The *g*-factors were obtained from Raman signal of S-NAC and R-NAC at 3371 cm^{-1}. All the *g*-factors of SERS-ChA were higher than 1.85 and remain a relatively stable value of 1.91 (r^2=0.999).

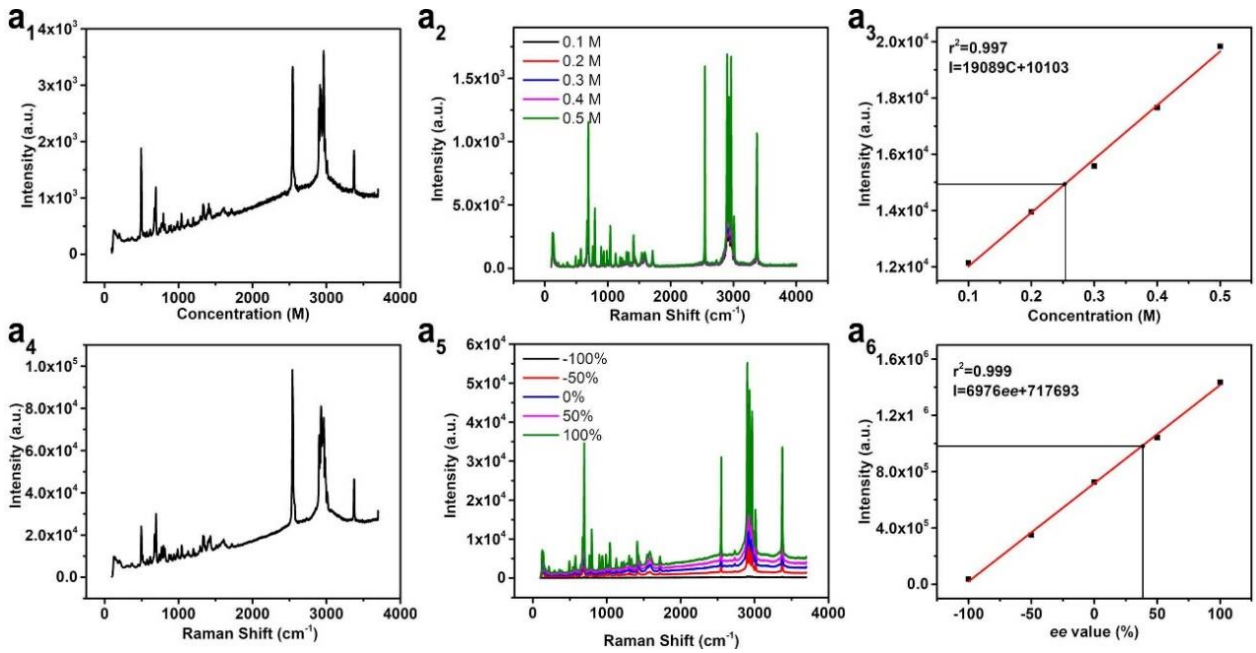

Figure S13. SERS-ChA effect of real-world samples prepared with multiple racemic interfering chemicals.

It is well known that other chiral, achiral or racemic molecules/intermediates in the real-world samples would be the main interference in Raman spectra.

As an example with racemic molecules, NAC solution with the interference of racemic cysteine and racemic cystine has been studied as a simulated real-world sample. A sample was prepared by mixing 0.25 M NAC with *ee* value of +37% as substances, and 0.1 M racemic cysteine and 0.05 M racemic cystine as the interfering chemicals.

As mentioned in main text, to measure *ee* value by SERS-ChA, concentration of the sample should be identified first. Here, we determined the concentration of enantiomer by using SERS. Figure S12a_1 shows the Raman spectrum of the simulated real-world sample measured on achiral NAF. At first, to obtain standard working curve for measuring concentration, Raman spectra of racemic NAC with concentration of 0.1, 0.2, 0.3, 0.4 and 0.5 M was measured on achiral NAF (Figure S12a_2). Figure S12a_3 show that a regression equation obtained from the responses is linear over a concentration (Raman shift=2925 cm^{-1}, r^2=0.997) of NAC used on achiral NAF, from which the concentration of NAC was determined to be 0.2527 ±0.0075 M with the recovery of 101.1% and error of 1.1%.

Then the *ee* value of the simulated real-world sample has been identified using R-CNAF. Figure S12a_4 shows the Raman spectrum of the simulated real-world sample measured on R-CNAF. At first, standard working curve (Figure S12a_5) was prepared by measuring Raman spectra of NAC with *ee* value of -100%, -50%, 0%, 50% and 100% with the concentration of 0.2527 M on R-CNAF (Raman shift=2925 cm^{-1}, r^2=0.997). As shown in Figure S12a_6, the *ee* values of simulated real-world samples of 37.60% ±0.23% has been obtained from the standard working curve of SERS-ChA. The results measured by SERS-ChA was close to the true *ee* value of the simulated real-world sample with the recovery of 101.6% and error of 1.6%.

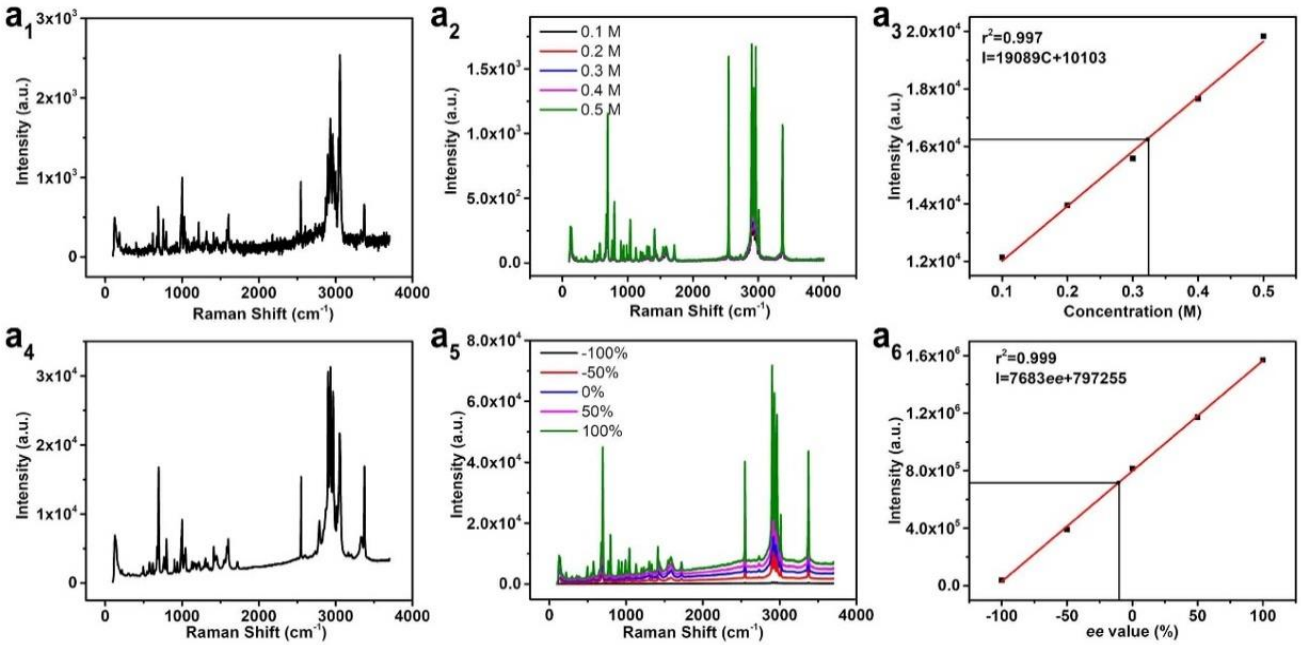

Figure S14. SERS-ChA effect of real-world samples prepared with multiple chiral interfering chemicals.

As another example of simulated real-world sample with multiple chiral interfering chemicals, NAC solution with the interference of (R, R)/(S, S)-Benzenemethanamine and (S)/(R)-N, α-Dimethylbenzylamine was investigated on R-CNAF.

A sample was prepared by mixing 0.3 M NAC solution with *ee* value of -12% as substances and a mixture of 0.1 M (R, R)/(S, S)-Benzenemethanamine with *ee* value of -100% and 0.05 M (S)/(R)-N, α-Dimethylbenzylamine with ee value of +50% as the interfering chemicals.

The concentration of enantiomer was determined by using SERS, at first. Figure S13a$_1$ shows the Raman spectrum of the simulated real-world sample measured on achiral NAF. To obtain the standard working curve for measuring concentration, Raman spectra of racemic NAC with concentration of 0.1, 0.2, 0.3, 0.4 and 0.5 M was measured on achiral NAF (Figure S13a$_2$). Figure S13a$_3$ shows that a regression equation obtained from the responses is linear over a concentration (Raman shift=2925 cm^{-1}, r^2=0.997) of NAC used on achiral NAF, from which the concentration of NAC was determined to be 0.3230 ±0.0078 M with the recovery of 100.9% and error of 0.9%.

Then the *ee* value of the simulated real-world sample has been identified using R-CNAF. Figure S13a$_4$ shows the Raman spectrum of the simulated real-world sample measured on R-CNAF. At first, standard working curve (Figure S13a$_5$) was prepared by measuring Raman spectra of NAC with *ee* value of -100%, -50%, 0%, 50% and 100% at the concentration of 0.3230 M on R-CNAF (Raman shift=2925 cm^{-1}, r^2=0.999). As shown in Figure S13a$_6$, the *ee* values of simulated real-world samples of -11.49% ±0.21% has been obtained from the standard working curve. The results measured by SERS-ChA was close to the true *ee* value of the simulated real-world sample with the recovery of 95.7% and error of 4.3%. Consequently, it can be considered that SERS-ChA on CNAF has good anti-interference ability.

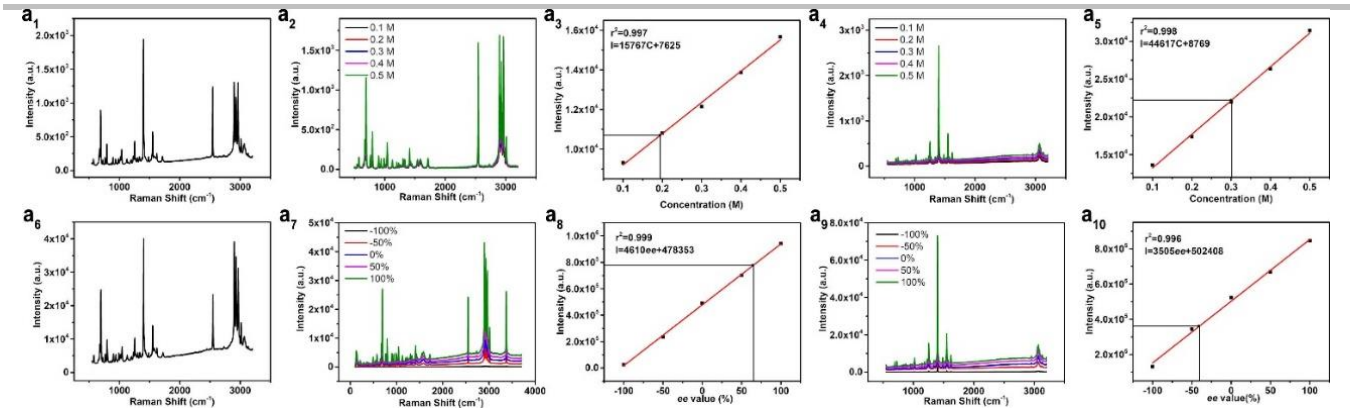

Figure S15. SERS-ChA effect of discriminating two enantiomers in one solution.

For the further purpose of the practical application of SERS-ChA, a complicated system with different enantiomers in one solution was detected.

A mixture solution of 0.2 M NAC with *ee* value of +67% and 0.3 M (S)/(R)-2,2,2-Trifluoro-1-(9-anthryl)ethanol with *ee* value of -41% solution was prepared for detecting each *ee* value.

To measure each *ee* value in a complicated system with different enantiomers, concentrations of each enantiomer should also be identified. Here, we determined the concentrations of enantiomers by using SERS. Figure S14a$_1$ shows the Raman spectrum of the simulated real-world sample measured on achiral NAF. At first, to obtain standard working curves for measuring concentrations, Raman spectra of racemic NAC (Figure S14a$_2$) and 2,2,2-Trifluoro-1-(9-anthryl)ethanol (Figure S14a$_4$) with concentration of 0.1, 0.2, 0.3, 0.4 and 0.5 M was measured on achiral NAF, respectively. Figure S14a$_3$ and Figure S15a$_5$ show that two regression equations obtained from the responses are linear over concentrations of NAC (Raman shift=2543 cm^{-1}, r^2=0.997) and 2,2,2-Trifluoro-1-(9-anthryl)ethanol (Raman shift=1400 cm^{-1}, r^2=0.998) on achiral NAF, from which the concentrations of NAC and 2,2,2-Trifluoro-1-(9-anthryl)ethanol were determined to be 0.1924 ±0.0038 M and 0.3012 ±0.0047 M with the recovery of 96.2% and 100.4% and error of 4.8% and 0.4%, respectively.

Then the *ee* value of the simulated real-world sample can be identified using R-CNAF. Figure S14a$_6$ shows the Raman spectrum of the simulated real-world sample measured on R-CNAF. At first, standard working curves were prepared by measuring Raman spectra of NAC (Figure S14a$_7$, Raman shift=2543 cm^{-1}, r^2=0.999) and 2,2,2-Trifluoro-1-(9-anthryl)ethanol (Figure S14a$_9$, Raman shift=1400 cm^{-1}, r^2=0.997) with *ee* value of -100%, -50%, 0%, 50% and 100% at the concentration of 0.1924 M and 0.3012 M on R-CNAF, respectively. As shown in Figure S14a$_8$ and Figure S14a$_{10}$, the *ee* values of NAC and 2,2,2-Trifluoro-1-(9-anthryl)ethanol in the simulated real-world samples was +65.42% ±0.18% and -41.77% ±0.23%, respectively, which have been obtained from the standard working curves. The results measured by SERS-ChA was close to the true *ee* value of NAC and 2,2,2-Trifluoro-1-(9-anthryl)ethanol in the simulated real-world sample with the recovery of 97.7% and 101.9%, and error of 2.3% and 1.9%, respectively.

Consequently, it can be considered that SERS-ChA on CNAF could discriminate two enantiomers at the same time.

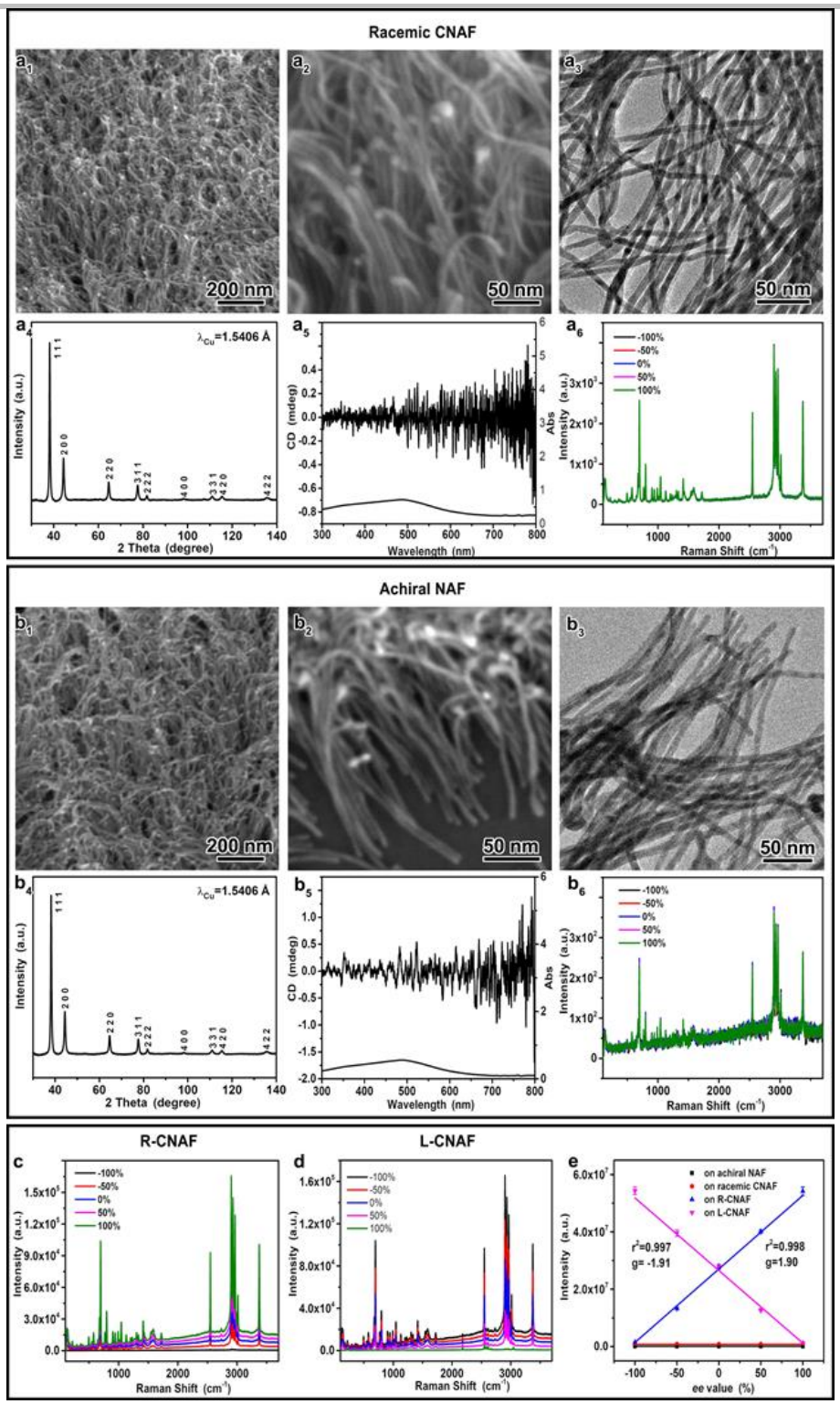

Figure S16. Characterization and SERS-ChA effects of racemic CNAFs (a), achiral NAFs (b), R-CNAFs (c) and L-CNAFs (d). SERS-ChA effects were detected by measuring the Raman spectra of S/R-NAC samples with *ee* values of -100%, -50%, 0%, 50% and 100%. **a_1, a_2, a_3, a_4, a_5, a_6,** Low-magnification SEM image, high-magnification SEM image, TEM image, XRD pattern, CD and absorbance spectra of racemic CNAFs, and Raman spectra measured on racemic CNAFs, respectively. **b_1, b_2, b_3, b_4, b_5, b_6,** Low-magnification SEM image, high-magnification SEM image, TEM image, XRD pattern, CD and absorbance spectra of achiral NAFs, and Raman spectra of achiral NAFs, respectively. **c,** Raman spectra of the R-CNAFs. **d,** Raman spectra of the L-CNAFs. **e,** Linear curves at a Raman shift of 2930 cm^{-1} for racemic CNAFs, achiral NAFs, R-CNAFs, and L-CNAFs. The average diameters of racemic CNAFs and achiral NAFs measured 5.4 (4.1–6.5 nm) and 5.5 nm (4.5–6.3 nm), respectively. The nanofibres in racemic CNAFs and achiral NAFs showed a straight morphology with a single crystalline structure (including BCB structure) with fewer defects than the other samples, which led to fewer hot spots for Raman enhancement.

No SERS-ChA effects were observed in either achiral NAFs or racemic CNAFs, while Raman scattering was *ca.* six times stronger on racemic CNAFs than on achiral NAFs. R-CNAFs and L-CNAFs showed a completely reversed SERS-ChA effect with *g*-factors of 1.90 and -1.91 for S/R-NAC, respectively.

Racemic CNAFs and achiral NAFs were synthesized according to the same preparation process as R-CNAFs except that 3.45 mM NAC (S-NAC: R-NAC=1:1) was used instead of S-NAC and S-NAC was not used.

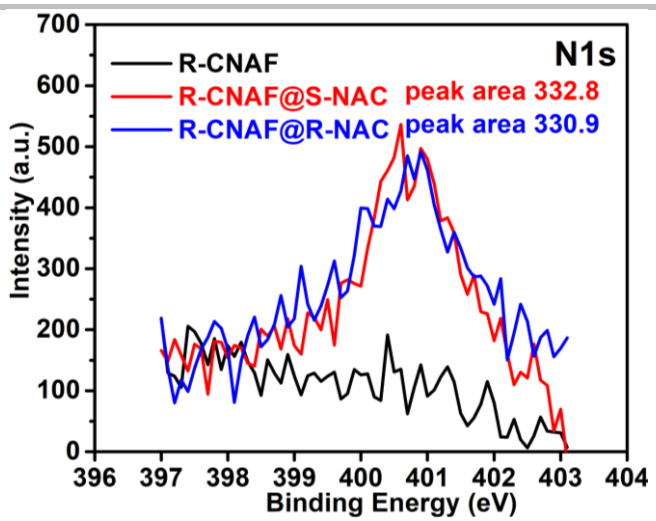

Figure S17. Chemical adsorption behaviour and optical properties of CNAFs. N1s XPS spectra of R-CNAFs before and after soaking in S-NAC (red line) and R-NAC (blue line).

XPS Spectra of R-CNAF@S/R-NAC were obtained on a SPECS XPS with soaking R-CNAF in S/R-NAC aqueous solution (0.3 M) for 30 min, then washed in ultrapure water and dried by a heat blower before putting into the XPS chamber. XPS spectrum of R-CNAFs showed no peaks, indicating the absence of organics in R-CNAFs. After adsorption of S/R-NAC, N1s spectra of R-CNAF@S/R-NAC showed single peaks at 400-401 eV with almost equal peak area of 332.8 and 330.9, respectively, showing no enantiomeric selectivity upon chemical adsorption in R-CNAF.

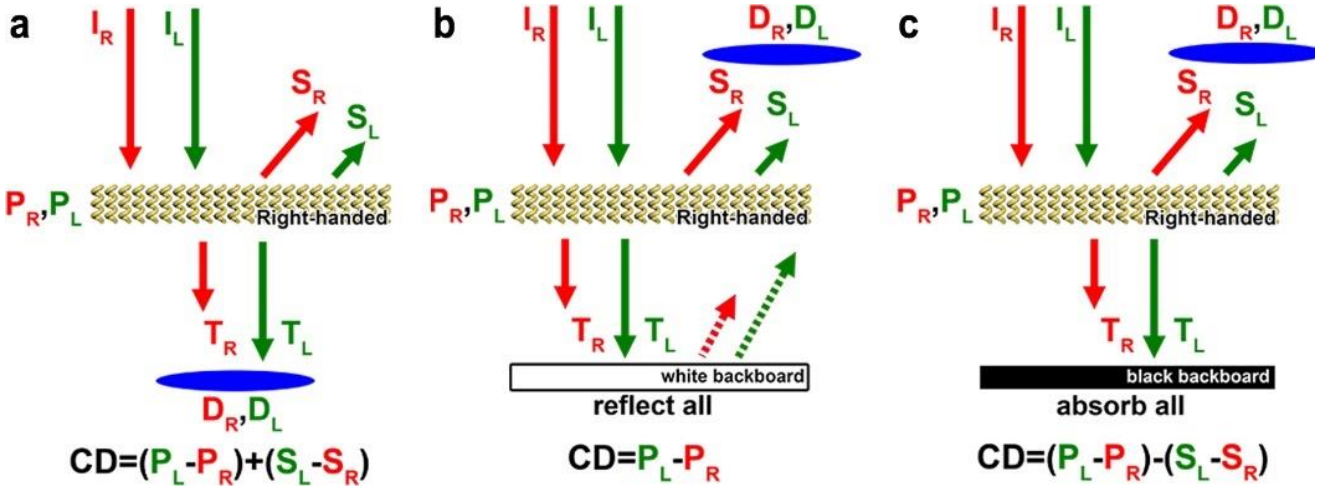

Figure S18. Chiral configuration of CNAFs. UV-Vis and CD spectra and schematic illustration of R-CNAFs grown on quartz substrate in transmission **(a)** and diffuse-reflectance modes with white **(b)** and black **(c)** backgrounds. Red and green arrows represent to right and left polarized light, respectively. *I* is the incident light (I_L=I_R), *P* is the plasmonic absorbed light, *T* is the transmitted light, *S* is the reflected light, and *D* is the detected light.

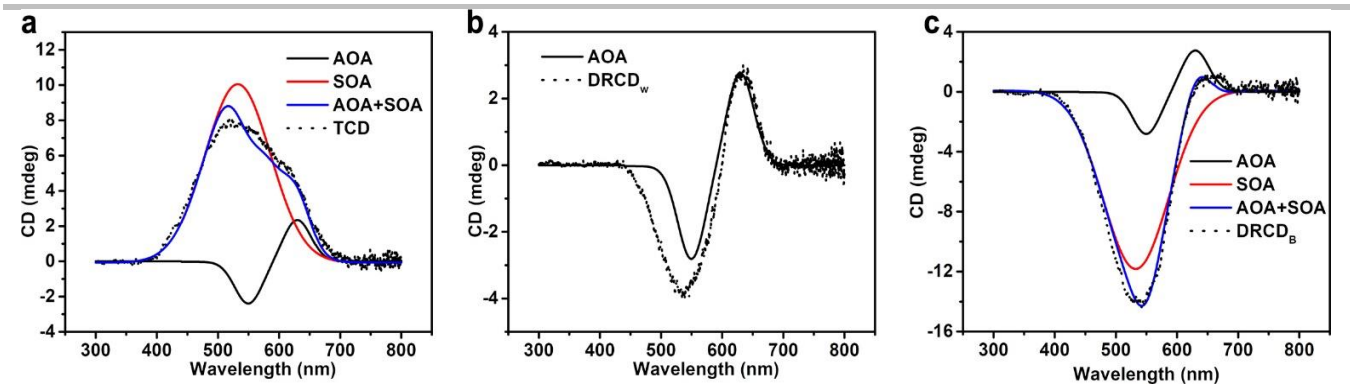

Figure S19. Illustration of chirality and OAs of chiral structure in R-CNAF. a, TCD. **b,** $DRCD_W$. **c,** $DRCD_B$.

TCD and DRCD spectra were analyzed through simulating AOA and SOA. $DRCD_W$ signal was generated all by AOA. $DRCD_B$ signals were generated through the combination of negative SOA and positive AOA. TCD signals were generated through the combination of both positive SOA and analogical positive AOA.

To confirm the chiral configurations of CNAFs and the corresponding generation of circular polarization in the CNAFs, OAs were unambiguously detected by CD spectroscopy. Figure S18 shows the UV-Vis and CD spectra of R-CNAFs grown on transparent quartz wafers. It is known that a medium with right-handed structures prefers to reflect right-handed circularly polarized light and absorb left-handed circularly polarized light. The TCD spectrum shows a positive main peak at ~514 nm, which confirms the right-handed configurations of R-CNAFs. The $DRCD_W$ displays positive exciton coupling at 460-650 nm. According to the CD detection mechanism illustrated in the Figure S17b some of the incident beams excite the plasmonic resonance of Au; some are scattered and detected, including normal diffuse reflection and circularly polarized Bragg resonance-based reflection; and the remainder pass through the CNAFs and substrate into the white background, which will be reflected by the white backboard and finally reach the detector after countless reflections. Thus, the $DRCD_W$ shows only the plasmonic absorption of CNAFs, indicating the handedness of CNAFs. As illustrated in the Figure S17c, transmitted light will be totally absorbed by the black backboard. The $DRCD_B$ spectra confirmed the presence of both plasmonic absorption- and scattering-based OA. $DRCD_B$ spectrum exhibits a negative signal at *ca*. 500 nm originating from the plasmonic absorption- and scattering-based OA by right-handed helical structures.

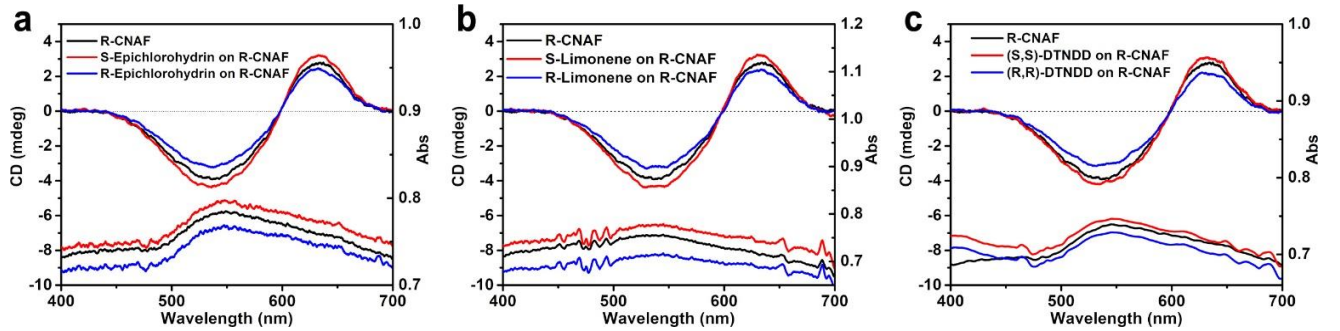

Figure S20. UV-Vis and DRCDW spectra of R-CNAFs without and with loading enantiomers. a, Epichlorohydrin. b, Limonene. c, DTNDD.

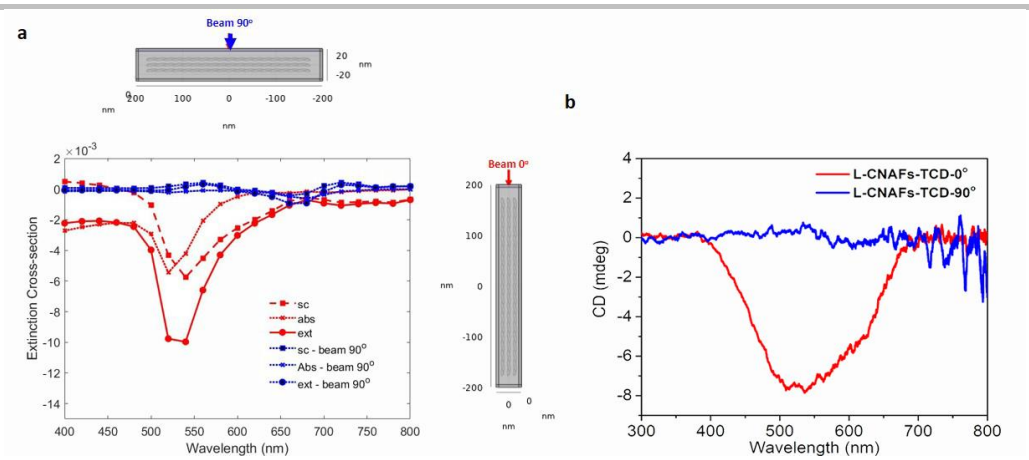

Figure S21. a, Simulated CD spectrum (extinction cross-section) and the corresponding contribution of scattering and absorption cross-section for a 3x3 array of L-tetrahelices with center-center separation of 12 nm. Red curves indicate the spectra when the propagation axis of the polarized light wave is parallel to the long-axis of the helices. Blue curves indicate the spectra when the propagation is perpendicular to the long axis of the helices. b, Experimentally obtained spectra for L-CNAFs in parallel and perpendicular orientation.

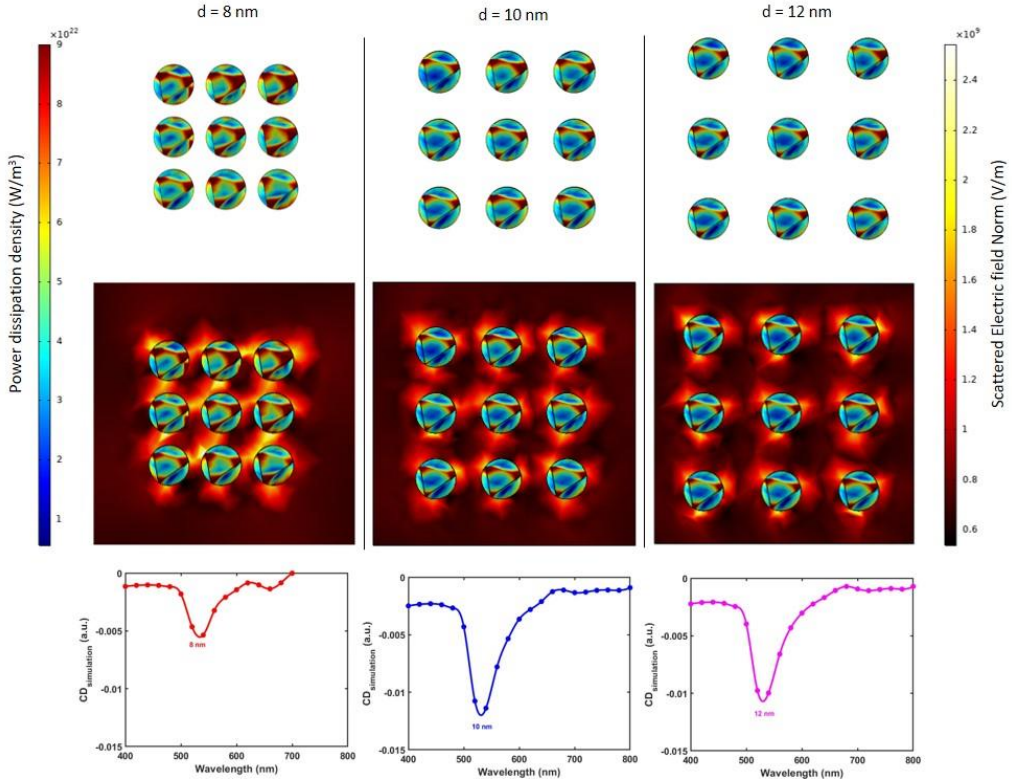

Figure S22. Effect of separation between tetrahelices. (top row) Simulated power dissipation density, (middle row) Scattered electric field around the tetrahelices and (bottom row) CD spectra obtained by subtracting extinction cross-section between L-CP light and R-CP light for left handed tetrahelices. Wavelength of incident CP light is 540 nm for top and middle rows. We observe that as the helices come closer they effect the interaction with CP light resulting in stronger absorption and scattering.

Reference

[1] D. Gangopadhyay, M. Das, K. K. Singh, P. Sharma, R. K. Singh, P. Tandon, *J. Phys. Chem. B* **2018**, *122*, 10306-10314.
[2] P. Oleynikov, *Cryst. Res. Technol.* **2011**, *46*, 569-579.
[3] a) C. C. Rullich, J. Kiefer, *Analyst* **2018**, *143*, 3040-3048; b) V. F. Kalasinsky, C. J. Wurrey, *J. Raman Spectrosc.* **1980**, *9*, 315-323; c) J. R. A. Moreno, F. P. Urena, J. J. L. Gonzalez, *Phys. Chem. Chem. Phys.* **2009**, *11*, 2459-2467.